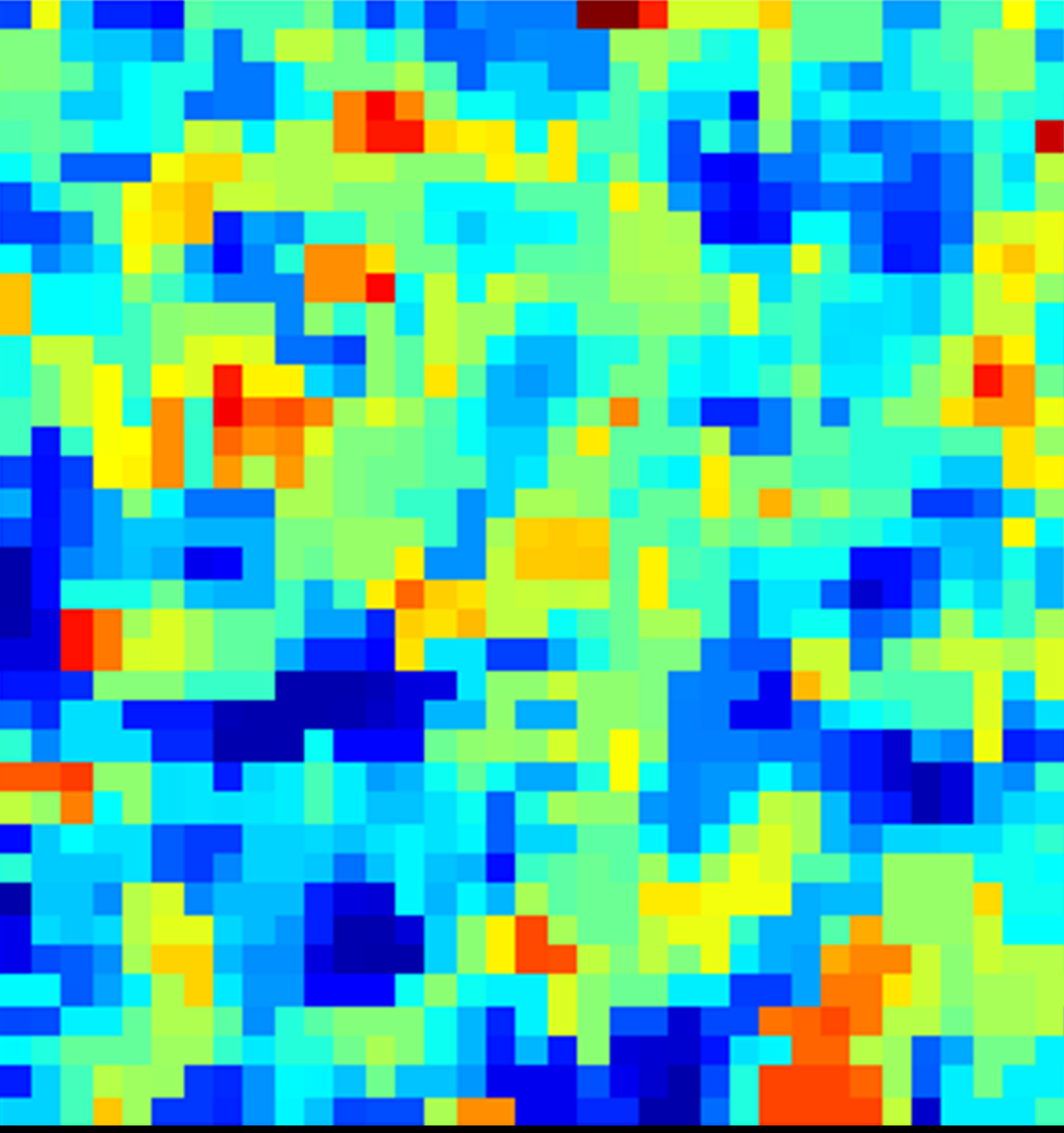

Optical Mapping of Isotonically Contracting Living Myocardial Slices: A Proof-of-Principle

Bian Renee Everts

Optical Mapping of Isotonically Contracting Living Myocardial Slices: A Proof-of-Principle

B.R. (Bian) Everts

Technical Medicine | Medical Imaging & Interventions

A thesis presented for
the degree Master of Science

Masters Graduation Committee

Chair	Prof. dr. M.M.A.E. Claessens Nanobiophysics University of Twente, Enschede, The Netherlands
Clinical supervisor	Dr. Y.J.H.J. Taverne Department of Cardiothoracic Surgery Erasmus University Medical Center, Rotterdam, The Netherlands
Supervisor	Prof. dr. N.M.S. de Groot Department of Cardiology Erasmus University Medical Center, Rotterdam, The Netherlands
Technological supervisor	Dr. C. Blum Nanobiophysics University of Twente, Enschede, The Netherlands
Process supervisor	Drs. P.A. van Katwijk Technical Medicine University of Twente, Enschede, The Netherlands
Daily supervisor	Drs. M.S. van Schie Department of Cardiology Erasmus University Medical Center, Rotterdam, The Netherlands
External Member	Prof. dr. P.C.J.J. Passier Applied Stem Cell Technology University of Twente, Enschede, The Netherlands

UNIVERSITY OF TWENTE.

Erasmus MC
University Medical Center Rotterdam

Preface

During the past year, I have been working on my Master's thesis for Technical Medicine. This thesis is the product of my labour over the past year.

I would like to thank prof. dr. Natasja de Groot for welcoming me to the department of translational electrophysiology at the Erasmus Medical Center. I am very grateful for the enthusiasm and guidance given to me by dr. Yannick Taverne. I appreciate that drs. Mathijs van Schie always had his door open for me. Thank you, dr. Christian Blum, for our three-weekly chats and your valuable feedback.

Many thanks to all my supervisors for all the freedom and trust that you have given me to do as I saw fit. This has helped me grow and become more secure in decision-making.

Also, thank you to prof. dr. Mireille Claessens for being the chair of my graduation committee and to prof. dr. Robert Passier for being the external member of the committee.

Finally, a big thank you to drs. Paul van Katwijk for being my mentor for the past two years. Together with our intervision group, you asked the right questions and gave me the space to grow as a professional and as a person.

Summary

Introduction Cardiovascular disease (CVD) poses a great health burden. However, the underlying causes of CVD, such as disturbances in action potential (AP) generation and propagation, and excitation-contraction coupling (ECC) are currently poorly understood. Many *in vitro* methodologies are available to study cardiac electrophysiology and ECC, each having its own limitations. This thesis aims to provide a new experimental setup to study cardiac electro(patho-)physiology in isotonically contracting myocardial slices (LMS), namely: motion-corrected optical mapping.

Methods Based on current literature, criteria for the optical mapping system were determined. The newly acquired optical mapping system was used to perform proof-of-principle experiments. Marker-based image registration and excitation ratiometry were used to reduce motion artefacts. Images were acquired at 2000 frames per second to record the rapid upstroke of the AP.

Results An optical mapping system for isotonically contracting LMS was built. Affine image registration was based on linearly moving markers. Excitation ratiometry was achieved through TTL-pulse synchronisation of the light sources and camera. The first ever optical mapping experiments on isotonically contracting LMS were performed. Optical mapping could be combined with contractile force measurements.

Conclusion This thesis provides the framework for the first optical mapping experiments on isotonically contracting LMS. Based on the preliminary results, optical mapping has the potential to become an invaluable tool in deciphering questions related to AP generation, propagation, and ECC.

Indexing Terms Arrhythmia – Electrophysiology – Excitation-Contraction Coupling – Heart Failure – Living Myocardial Slices – Motion Correction – Optical Mapping – Ratiometry

Contents

List of Abbreviations

AF	**A**trial **F**ibrillation
AP	**A**ction **P**otential
APD	**A**ction **P**otential **D**uratoin
AV	**A**trio**v**entricular
BDM	2,3-**b**utane**d**ione **m**onoxime
BMCC	**B**io**m**imetic **C**ulture **C**hamber
bpm	**b**eats **p**er **m**inute
CaT	**C**alcium **T**ransient
CCD	**C**harge **C**oupled **D**evice
CICR	**C**alcium-**I**nduced **C**alcium **R**elease
CMOS	**C**omplementary **M**etal-**O**xide **S**emiconductor
CSD	**C**alcium **S**ensitive **D**ye
CV	**C**onduction **V**elocity
CVD	**C**ardio**v**ascular **D**isease
ECC	**E**xcitation-**C**ontraction **C**oupling
fps	**f**rames **p**er **s**econd
FOV	**F**ield **O**f **V**iew
FWHM	**F**ull **W**idth **H**alf **M**aximum
HF	**H**eart **F**ailure
$\mathbf{I}_{Ca}$	**C**a^{2+} **C**urrent
$\mathbf{I}_{f}$	**F**unny **C**urrent
$\mathbf{I}_{K}$	**K**$^{+}$ **C**urrent
$\mathbf{I}_{Na}$	**N**a^{+} **C**urrent
LA	**L**eft **A**trium
LED	**L**ight-**E**mitting **D**iode
LMS	**L**iving **M**yocardial **S**lices
MEA	**M**ulti-**E**lectrode **A**rray
OAP	**O**ptical **A**ction **P**otential
QY	**Q**uantum **Y**ield

RA	**R**ight **A**trium
ROI	**R**egion **O**f **I**nterest
ROS	**R**eactive **O**xygen **S**pecies
RyR	**Ry**anodine **R**eceptors
SA	**S**ino**a**trial
SNR	**S**ignal to **N**oise **R**atio
SR	**S**acroplasmic **R**eticulum
TTL	**T**ransisitor-**T**ransistor **L**ogic
UV	**U**ltra**v**iolet
VF	**V**entricular **F**ibrillation
$\mathbf{V}_m$	**M**embrane **P**otential
VSD	**V**oltage **S**ensitive **D**ye
VT	**V**entricular **T**achycardia
$\mathbf{S}_0$	singlet ground state
$\mathbf{S}_1$	first singlet excited state
2D	**T**wo-**D**imensional
3D	**T**hree-**D**imensional
$\Delta\mathbf{F}$	change in fluorescence intensity

1 Introduction

1.1 Overview

Cardiac arrhythmias and cardiovascular disease (CVD) pose a great health burden. Arrhythmias can cause sudden death, stroke, or heart failure (HF) [1]. Cardiac arrhythmias are caused by disturbances in the activation and recovery of electrical excitation through the myocardium [2]. However, causes for disturbances in cardiac action potential (AP) generation and propagation in conditions such as atrial fibrillation (AF) and HF are currently poorly understood [3]. It is of great importance to gain more insight into cardiac electrical activity and excitation-contraction coupling (ECC) to gain a better understanding of the mechanisms behind these conditions and, ultimately, to gain insight into methods for an effective treatment.

Many *in vitro* cardiac models are available to study CVD, varying from isolated cardiomyocytes [4] and engineered heart tissue [5] to coronary-perfused ventricular wedge preparations [6] and Langendorff-perfused hearts [7, 8]. These models are simplifications of reality, each having its limitations. Isolated cardiomyocytes lack physiologically relevant conditions and environmental cues, leading to cardiac dedifferentiation [9–11]. It is difficult to advance the maturation of engineered heart tissue to an adult-like structure and function [10–12]. Cardiac wedges and Langendorff-perfused hearts are complicated and expensive setups requiring coronary perfusion, study time is limited to several hours, and exclusively non-human tissue is used [7, 8, 11, 12].

Living myocardial slices (LMS) overcome most of the aforementioned limitations [10, 12–16]. LMS are ultrathin (~300 μm) living sections of cardiac tissue. The normal tissue architecture [15], multicellular environment [15, 17], and three-dimensional (3D) tissue structure [18] are preserved, resulting in normal contractility [18, 19], electrophysiological properties [15, 16, 18], and intracellular calcium dynamics [13, 17]. Advances in biomimetic electromechanical stimulation and specific physiological preload have resulted in more stable *in vitro* models in which cardiac dedifferentiation is prevented [18, 19]. These combined features make LMS suitable for *in vitro* cardiac electrophysiological investigations [20]. At the translational electrophysiology laboratory of the Erasmus Medical Centre, equipment is available to produce and culture LMS in biomimetic culture chambers (BMCC).

Until recently, most electrophysiological research relied on multi-electrode mapping techniques [16, 17, 21, 22], which are limited by the relatively low electrode density and are unable to capture AP morphology [11, 23]. Furthermore, activation mapping

data can be ambiguous during fibrillation due to multiple sharp deflections, low amplitude, and artefacts [24].

An alternative for multi-electrode mapping techniques is optical mapping. With fluorescent probes, optical mapping allows the imaging of electrical activation and repolarization at high spatial resolutions [3, 23]. Furthermore, optical mapping enables the visualisation of sodium, potassium, and calcium transients (CaT) [25].

The recent advances in LMS and optical mapping make it possible to conduct *in vitro* experiments on living human cardiac tissue. Commonly, pharmacologic agents are used for electromechanical uncoupling. Uncoupling is done to eliminate motion artefacts caused by the contracting tissue. However, cardiac electrophysiology is altered by administering such pharmacologic agents, making the studies less representable for *in vivo* translation [26, 27]. Additionally, electromechanical uncoupling impedes the investigation of ECC. Ratiometric imaging [28] and image registration [29] could partially correct the motion artefacts caused by contractions. Recent studies by Zhang *et al.* and Kappadan *et al.* have combined these techniques, making it possible to optically map contracting cardiac tissue [26, 30].

1.2 Aim of the Study

Until now, optical mapping studies on LMS have been performed on mechanically restrained or electro-mechanically uncoupled preparations. This thesis aims to provide the first experimental setup in which optical mapping and isotonic force contraction measurements are performed simultaneously on human LMS in a BMCC. The combination of biomimetic LMS culturing and motion-corrected optical mapping could provide insight into AP conduction and morphology, and calcium handling, in contracting cardiac tissue while closely mimicking *in vivo* conditions. Measurement of these parameters alongside cardiac contractile force measurements could be a stepping-stone towards a better understanding of cardiac electro(patho-)physiology. This could help further research into arrhythmias and HF by unravelling the relationship between contractile dysfunction, calcium handling, and AP conduction.

1.3 Thesis Structure

Chapter 2 provides the reader with more in-depth background information on cardiac anatomy and physiology, LMS, and optical mapping. In the following chapter, the requirements for the optical mapping system are discussed. This is followed by the methodology for data acquisition, processing, and analysis in *Chapter* 4. Results of the optical mapping system and preliminary experiments are presented in *Chapter* 5. In the final chapter, a general discussion and conclusion are drawn.

Background Information 2

This chapter aims to provide the reader with background information for the rest of the thesis. First, the anatomy, electrophysiology, and pathology of the heart are discussed. Next, an introduction is given to the preparation of LMS and the advances in BMCCs. Finally, the basic principles of optical mapping and fluorescence are explained. The focus is placed on the mechanisms behind fluorescence and ratiometric imaging, optical mapping instrumentation, and the main fluorophores used in cardiac optical mapping.

2.1 The Heart

In short, the heart is a double, self-adjusting suction and pressure pump (see *Figure* 2.1). The right side of the heart receives poorly oxygenated venous blood from the systemic circulation and pumps this through the pulmonary circulation, where the blood is oxygenated by the lungs. The left side of the heart receives oxygenated blood from the pulmonary circulation and pumps it into the aorta to be distributed into the systemic circulation. [31, 32]

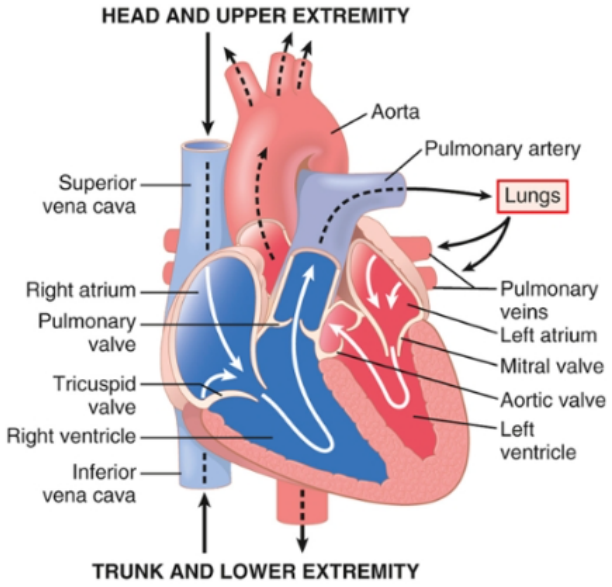

FIGURE 2.1: Anatomy of heart [32].

The heart consists of four chambers: the right and left atria, and the right and left ventricles. The atria receive blood from the circulation and pump this into the ventricles. The tricuspid- and mitral valve, present in the right and left atrioventricular (AV) orifice, respectively, prevent the backflow of blood from the ventricles to the atria during ventricular contraction (systole). The pulmonary and aortic valves prevent the backflow of blood from their outflow tracts into the ventricles during ventricular relaxation (diastole). [32, 33]

2.1.1 Electrophysiology

The heart's electrical activity originates from the sinoatrial (SA) node in the right atrium (RA). These cells depolarize spontaneously at a rate between 60 and 100 beats per minute (bpm). The generated AP propagates from the SA node through the right atrial myocardium, through gap junctions, and spreads to the left atrium (LA). A fibrous AV ring prevents AP conduction from the atria to the ventricles. A specialized conducting network, the AV-node and His-Purkinje fibre system, allows the conduction of the AP to the ventricles. *Figure* 2.2 shows the anatomy of the electrical system of the heart. Due to a short delay in the AP propagation in the AV-node, the atria contract before the ventricles, allowing the atria to empty into the ventricles. The His bundle and Purkinje fibres rapidly distribute the AP throughout the ventricles, causing an orderly contraction of the ventricles. [32, 34, 35]

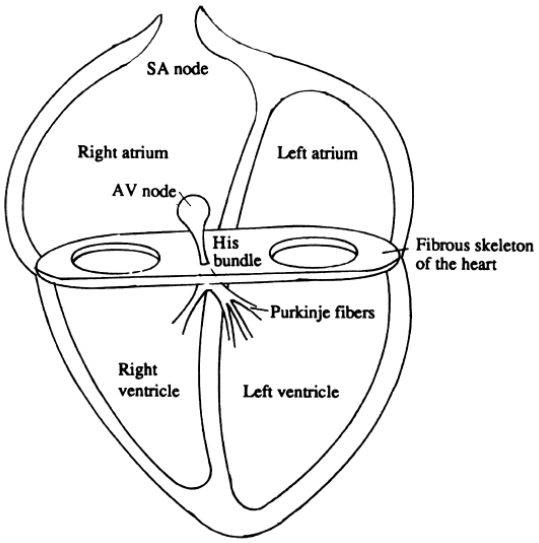

FIGURE 2.2: Anatomy of the electrical system of the heart [34].

2.1.2 The Cardiac Action Potential

The inside of cardiac cells has a negative electrical charge compared to the outside. The resting membrane potential (V_m) of atrial and ventricular cardiomyocytes is -80 to -90 mV. When a cell depolarizes and reaches its threshold, Na^+ and Ca^{2+} channels open. A positive charge enters the cell, depolarizing the cell further. A positive intracellular current is produced, depolarizing adjacent cells through gap junctions. [32, 35]

The underlying mechanism for the cardiac AP is based on four time-dependent, voltage-gated membrane currents: the Na^+ current (I_{Na}), Ca^{2+} current (I_{Ca}), K^+ current (I_K), and the pacemaker or funny current (I_f). The initiation time, shape,

and duration of an AP are distinctive for five regions of the heart: the SA node, atrial muscle, AV node, Purkinje fibres, and ventricular muscle. The differences in AP shape are caused by varying ion-channel characteristics in the distinct regions. Below, the general mechanisms behind the cardiac AP in ventricular and atrial muscle are described. [32, 35]

The atrial and ventricular AP depend on I_{Na}, I_{Ca}, and I_K. The rapid upstroke of the cardiac AP is caused by the opening of voltage-activated fast Na^+ channels (fast sodium channels) and slow L-type Ca^{2+} channels (slow calcium channels). This process results in distinctive voltage changes, as graphed for a ventricular AP in *Figure* 2.3, along with the corresponding ionic currents. The depolarization (*phase 0*) consists of the opening of the fast sodium channels, which allows the V_m to rapidly (in 1 to 2 *ms*) become more positive [36]. Once the fast sodium channels close (*phase 1*), the cell begins to repolarize. Meanwhile, the slow calcium channels open and remain open for several tenths of a second, maintaining a plateau in the AP (*phase 2*). The Ca^{2+} ions entering the cell activate the muscle contractile process. Immediately after the onset of the AP, K^+ permeability is decreased, preventing the V_m from returning to its resting potential. Once the slow calcium channels close, K^+ permeability increases rapidly, allowing the V_m to return to its resting level (*phase 3*). When repolarization has occurred, the cell remains in its resting phase (*phase 4*) until it is excited again. [32, 35]

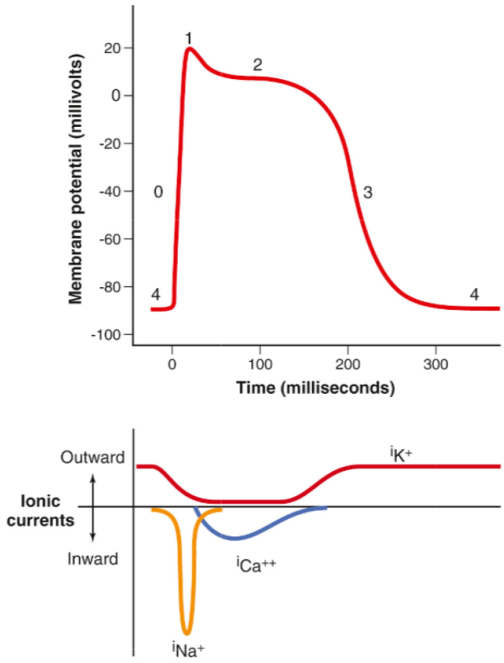

FIGURE 2.3: Ventricular cardiac action potential and its associated ion currents [32].

Once a cell is depolarized, it cannot be depolarized again until repolarization has occurred. This is called the refractory period. The refractory period lasts from the end of phase 0 until late into phase 3. [32, 35]

2.1.3 Excitation-Contraction Coupling

Cardiac muscle contraction is initiated by electrical excitation from the SA node. The propagating AP causes myofibrils to contract. This is referred to as ECC. An AP

spreads to the interior of cardiomyocytes through transverse tubules (T-tubules). The T-tubules are an extension of the extracellular space. During depolarization, slow calcium channels on the T-tubule membrane facilitate the diffusion of Ca^{2+} throughout the cardiomyocytes. Each slow calcium channel controls a set of ryanodine receptors (RyR), or Ca^{2+}-release channels, on the sarcoplasmic reticulum (SR). In these dyadic spaces, the local interface between T-tubules and the SR, an increase in intracellular Ca^{2+} concentration ($[Ca^{2+}]_i$) causes calcium-induced calcium release (CICR) from the SR. This can be seen as a calcium spark. The spatial and temporal summation of many calcium sparks causes a significant increase in $[Ca^{2+}]_i$, which leads to muscle contraction. [32, 37, 38]

The increased $[Ca^{2+}]_i$ causes Ca^{2+} to bind to troponin-C, allowing cross-bridge formation and cycling between actin and myosin filaments. The sliding of actin and myosin filaments is what generates contractile force. The contractile force of the cardiac muscle is regulated by the rise of $[Ca^{2+}]_i$ and Ca^{2+}-sensitivity of regulatory proteins. At the end of the plateau phase, the calcium influx suddenly stops. Calcium ions are returned to the extracellular space and the SR, halting the contraction. Hence, the duration of the contraction depends on the duration of the AP. In atrial tissue, this is about 0.2 s. In ventricular tissue, this is about 0.3 s. [32, 37]

2.1.4 Arrhythmias and Heart Failure

Cardiomyocyte mishandling of Ca^{2+} is a central cause of contractile dysfunction and arrhythmias in pathophysiological conditions [39]. An arrhythmia is any heart rhythm other than the normal sinus rhythm generated by the SA node. Disruptions in the electrical excitation of the myocardium can lead to arrhythmias [2]. Cardiac arrhythmias have an expected prevalence of 1 to 5% in the adult population [40], with AF being the most common arrhythmia [41, 42]. AF is associated with increased mortality and an increased risk of HF, myocardial infarction, stroke, and gastrointestinal bleeding [1].

Heart failure is the inability of the heart to sufficiently provide blood and oxygen to peripheral tissues. HF is mainly caused by underlying cardiac conditions, such as valvular disease, endo- or pericardial abnormalities, or arrhythmias [43]. In the western world, the reported prevalence of HF varies from 1 to 12% [44]. Patients with HF have a poor prognosis, with a mortality rate of 25 to 50% within five years after HF has been diagnosed [43]. Alterations in ion channels [45] and dyadic structures [45, 46] are seen in HF, impairing ECC [47, 48]. Such alterations are either the cause of HF or an outcome caused by HF [43].

2.2 Living Myocardial Slices

LMS are ultra-thin living sections of heart tissue prepared with a vibratome. Due to their surface-to-thickness ratio, these 100 to 400 μm thick slices are considered pseudo-3D [13, 14]. LMS can be used as a translational research model between animal models and clinical studies in cardiac electrophysiology and pathology. For example, studies in electrophysiology, contractility, and arrhythmias can be performed on LMS [10, 12, 18]. An example of a LMS is shown in *Figure* 2.4.

LMS retain the cardiac tissue's native multicellular phenotype, 3D architecture and extracellular matrix, as well as electromechanical and biochemical properties [10, 13, 14]. This results in maintaining properties such as AP duration, contractility,

calcium handling, and conduction velocity (CV) [11, 16, 49]. With a maximal oxygen diffusion distance of 200 μm [50], the thinness of LMS allows the diffusion of oxygen and nutrients throughout the whole slice, preserving the viability of the slice without the need for coronary perfusion [10, 13–15, 19].

2.2.1 Preparation

The first LMS were described in the 1930s [51]. At the time, LMS were prepared with hand-held blades. Since then, vibratomes with a minimal Z-axis error (<1 μm [52]) and improved protocols have resulted in the current ultra-thin, precision-cut LMS we know today. By placing the tissue epicardial face down, trimming the tissue as flat as possible, and slicing tangentially to the epicardium, less than 3% of the cardiomyocytes is damaged [15, 17]. The damage is limited to the superior and inferior cell layers of the slices. Embedding cardiac tissue in low-melting agarose can help stabilize the vibratome during slicing, which is especially useful in fibrotic and fat-rich tissue. During the slicing procedure, the tissue is immersed in a 4°C Tyrode's buffer. This environment substantially lowers the tissue's energetic demands, minimizing the risk of ischemia. [52]

2.2.2 Biomimetic Culture Chamber

In a successful LMS, the myocardial phenotype has functional and structural features of fresh myocardium [13]. However, the prolonged culture of LMS results in an observable loss in structural and functional integrity. This is seen by a 90% decrease in contractile force and cardiomyocyte dedifferentiation. [12, 14, 53] A lack of mechanical preload and electrical stimulation forms the basis for the loss in contractility and dedifferentiation in LMS [12, 13, 18, 19, 54, 55]. This underlines the importance of a proper electrophysiological environment in the preservation of LMS function, which can be provided by BMCCs.

Cardiac culture systems aim to replicate key features of the *in vivo* environment. By replicating the *in vivo* environment, loss in contractile force and dedifferentiation

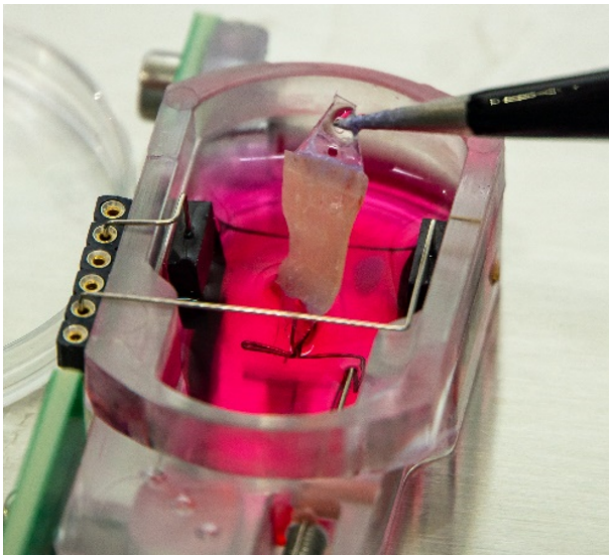

FIGURE 2.4: LMS, as prepared by the translational electrophysiology laboratory at the Erasmus Medical Center

are prevented. BMCCs include mechanical and electrical stimulation, oxygenation, and nutrient support of the LMS [13, 18, 19]. Recently, significant advances in slice culture were made. Qiao *et al*. [55] implemented a culture system that supports accurately controlled conditions with continuous O_2/CO_2 control, an orbital shaker, medium circulation, static mechanical loading, and electrical stimulation. They were able to maintain normal electrophysiology of human LMS for 4 days in a user-friendly platform. Fischer *et al*. [18] designed a BMCC that allows the culture of beating intact LMS under constant monitoring. Tissue function, structure, and differentiation were preserved for up to four months. This was achieved by elastic contraction, adequate O_2 delivery, and electrical stimulation.

2.3 Optical Mapping

In principle, optical imaging is based on wavelength-dependent light-tissue interactions. These interactions include photon scattering, total internal reflection, absorption, and reflectance [25]. Optical fluorescence mapping, or optical mapping, is a fluorescence-based optical imaging technique that enables studying cardiac electrophysiology with high spatial resolution [56]. To perform optical mapping, a fluorophore is added to a specimen. Upon excitation of the fluorophore, fluorescence occurs. The emitted fluorescence is captured by a photodetector. *Figure* 2.5 shows a schematic drawing of an optical mapping system.

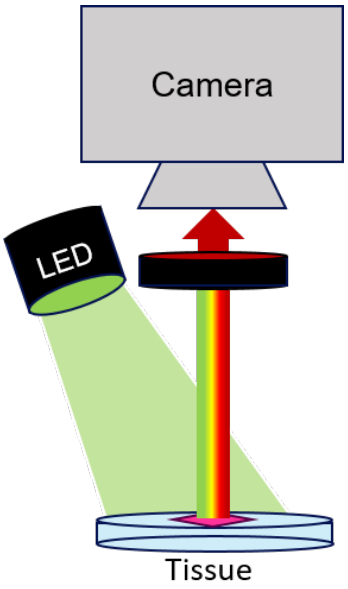

FIGURE 2.5: Schematic drawing of an optical mapping system with a tissue slice excited by an LED in the in the wavelength range of green light. Fluorescence is emitted in a broad spectrum of wavelengths, and filtered with a band-pass emission filter for red/near-infrared light.

Changes in fluorescence intensity (ΔF) have been used to measure a wide range of physiological parameters, including cellular metabolic state, membrane potential, intracellular ion concentrations, pH, and oxygen tension [25]. In cardiology, membrane potential and intracellular free calcium indicators have been the most important optical probes. Potentiometric, or voltage-sensitive dyes (VSDs), are used to record optical APs. Electrical activation, AP propagation, duration and

morphology, CV, and repolarization maps are acquired based on changes in fluorescence [3, 11, 25, 56]. Based on these parameters, AP upstroke analysis, arrhythmia analysis, and phase mapping can be performed [25, 57].

Intracellular calcium indicators are used to study changes in the kinetics and amplitude of calcium transients [58–60]. Calcium dynamics are displayed in colour-coded maps [61], which are used to interpret mechanisms of arrhythmias [62–64] and HF [65]. The calcium upstroke and extrusion phases and calcium transient time-to-peak are used to study the activity of cellular RyR. The calcium transients duration can be viewed as an analogue for the AP duration. Furthermore, calcium indicators are used to study calcium kinetics that influence contractility [61]. A combination of VSDs and calcium indicators gives insights into ECC and arrhythmia mechanisms [61].

Advantages of optical mapping over conventional electrode mapping are the high spatial resolution, the ability to simultaneously measure several physiological parameters, and the absence of artefacts due to electrical stimulation [23, 25, 56]. Furthermore, with optical mapping, it is possible to monitor multiple sites at once.

A major limitation of optical mapping is the spatial and temporal variation in fluorescence. The spatial variation is mainly caused by the motion of contracting tissue. Contraction causes the correlation between the tissue and the photodetector to be lost. *Figure* 2.6 shows an exaggeration of a motion artefact to explain the principle.

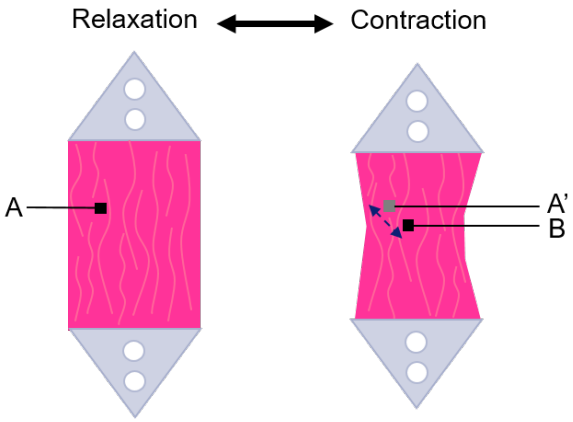

FIGURE 2.6: A schematic representation of a relaxed and contracted LMS. Black square *A* represents an area of tissue in a relaxed state, which is recorded by pixel *A*. Black square *B* represents the same portion of tissue during contraction, displaced to a different location, thus recorded by another pixel. Grey square *A'* represents the location of pixel A during contraction. The blue arrow shows the pixel displacement during contraction.

During relaxation, the fluorescence from a certain portion of the LMS is captured by pixel *A* of the photodetector, as shown by the black square in *Figure* 2.6. Once the LMS is contracting, the tissue is displaced: relative to the stationary photodetector, the tissue in location *A* is displaced to location *B* over time. The camera is recording the fluorescence at pixel *A'*, which is the original location of the tissue. Due to motion, the recorded fluorescence originates from a different location in tissue, making the recorded fluorescence a summation of fluorescence of multiple tissue locations over time.

Commonly, motion artefacts in LMS are suppressed by electromechanical uncouplers such as blebbistatin and 2,3-butanedione monoxime (BDM). The use of these uncouplers may result in alterations in AP duration and calcium handling [26]. Another solution for the reduction of artefacts is the use of motion-tracking algorithms in combination with ratiometric imaging, which has been applied in Langendorff perfused hearts [26, 28, 30].

Other causes for the variation in fluorescence are uneven distribution of the dye, heterogeneous tissue structure, uneven illumination, photobleaching, and dye washout [28, 61]. Variations in fluorescence can be corrected by ratiometric imaging. However, with optical mapping, it is not possible to provide an absolute value for V_m. Instead, a relative change in fluorescence intensity is recorded.

Finally, there has not been a consensus on the depth of field in optical mapping yet. However, ranges from 300 to 500 μm [66, 67], and ranges up to 2 mm [68] have been reported. In either case, it can be assumed that sufficient fluorescence can be recorded from LMS with a thickness of ~300 μm. It should be noted that every cell layer in a LMS contributes to the emitted fluorescence signal. Hence, the recorded fluorescence should be interpreted as an averaged signal throughout the slice thickness.

2.3.1 Fluorescence

Fluorescence is the light emitted by an atom or molecule, called a fluorophore, after the absorption of electromagnetic energy. Electromagnetic energy is absorbed and emitted in discrete amounts, known as quanta or photons [69]. Fluorescence arises from the transition of an excited fluorophore from its *first singlet excited state* (S_1) to its *singlet ground state* (S_0). [70] The process from absorption to emission of light can be schematically illustrated with a Jablonski diagram, as shown in *Figure* 2.7. The *singlet ground state* and *first singlet excited state* are shown as S_0 and S_1, respectively. At each energy level, a fluorophore can exist in several vibrational levels, here shown as 0, 1, 2, and 3. After light absorption, a fluorophore is excited from S_0 to a higher vibrational level in S_1. The fluorophore rapidly relaxes into the lowest vibrational level of S_1. This is called internal conversion or non-radiative transition. After internal conversion, fluorescence occurs as the fluorophore returns to S_0. Usually, the fluorophore relaxes to a higher vibrational level in the ground state. [71]

The energy of the emitted photon is lower than the energy of the absorbed photon: fluorescence occurs at lower energies, which translates to longer wavelengths. This phenomenon is called the Stokes shift. The Stokes shift is caused by internal conversion in S_1 and the return to a higher vibrational level in S_0. Both of these mechanisms result in the loss of excitation energy in the form of thermal energy. [71] The difference in energy between excitation light and fluorescence, caused by the Stokes shift, is the key to distinguishing between excitation light and fluorescence.

Two important characteristics of a fluorophore are its quantum yield (QY) and its fluorescence lifetime (τ). The QY of a fluorophore is the ratio between the number of emitted photons and the number of absorbed photons. The rate of the QY can be written as

$$\Phi = \frac{\Gamma}{\Gamma + k_{nr}}, \tag{2.1}$$

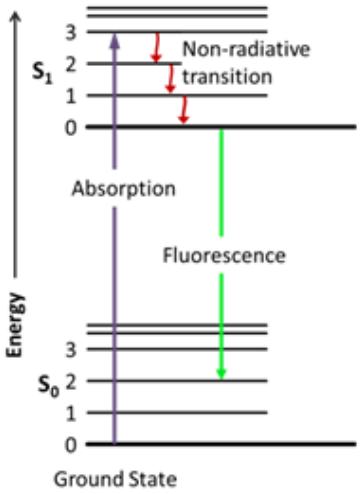

FIGURE 2.7: Jablonski diagram with two energy levels (S_0 and S_1), each containing four vibrational levels (0, 1, 2, and 3) [72].

where Γ is the radiative rate of the fluorophore and k_{nr} is the rate of non-radiative decay to S_0. Due to forms of non-radiative decay, Φ is always lower than 1. Fluorophores with a high QY show the brightest emissions and, thus, the highest intensity. The lifetime τ determines the time a fluorophore can interact with its environment. Generally, the lifetime τ is near 10 ns. It can be calculated according to

$$\tau = \frac{1}{\Gamma + k_{nr}} \,. \tag{2.2}$$

Several factors can cause the reduction of fluorescence intensity, or quenching. Examples of quenching mechanisms are molecular interactions, energy transfer, charge transfer, and photochemistry [73]. Furthermore, fluorophores are sensitive to photobleaching, especially under constant illumination [74]. Apart from quenching, some fluorophores present with changes in fluorescence intensity based on changes in V_m or ion concentrations [75]. These mechanisms are useful for tissue examination.

2.3.2 Optical Mapping Instrumentation

Cardiac optical mapping studies require VSDs and/or calcium indicators. Fluorescence, caused by the illumination of these fluorophores via an external light source, is recorded with an imaging system.

Lenses are used to maximize the effective numerical aperture (NA), light collection, and signal-to-noise ratio (SNR). Band-pass filters are used to capture a specific wavelength range of the emitted light [75]. Once the emitted light has passed the lens and filter, it is recorded by a photodetector or camera. Charge-coupled device (CCD) cameras and complementary metal-oxide semiconductor (CMOS) cameras are replacing photodiode arrays [76, 77]. Overall, camera use is shifting towards CMOS cameras because of their high-speed, low-light image acquisition. [77]

The acquired images are processed and analysed. Multiple research groups have shared their open-source software for the analysis of optical mapping data. O'Shea *et al.* [78] have created the open-source MATLAB-based ElectroMap software for the analysis of voltage and calcium optical mapping data [79]. In 2021, Tomek *et al.* released two identical versions of the open-source software: COSMAS, one MATLAB-based and one Python-based, for bulk analysis of optical mapping data [80]. Most recently, Cooper *et al.* released their open-source Python-based optical mapping analysis software *KairoSight*, which is a user-friendly platform [81].

2.3.3 Fluorophores

As stated before, cardiac optical mapping is mainly performed with VSDs and calcium indicators. VSDs anchor to the cell membrane. Many VSDs can rapidly follow changes in V_m, allowing the measurement of APs [3, 75, 82]. A change in fluorescence intensity occurs linearly to the change in V_m [76]. There are two possible mechanisms behind the spectral shift along with the change in V_m [75]. The electrochromic theory states that there is a coupling between V_m and the electronic states of the dye molecule. As the V_m changes, molecules in the VSD undergo an electronic redistribution, changing the electronic state of the molecules, which results in a linear change in fluorescence intensity upon excitation. The solvatochromic theory suggests that dye molecules are reoriented by a change in the electrical field. [75] *Figure* 2.8 schematically shows the spectral shift of a fluorophore that occurs in response to a change in V_m. The black line is the spectrum during the resting phase. The dashed grey line represents the spectral shift that occurs due to depolarization. At λ_1, the shift results in a decrease in fluorescence intensity.

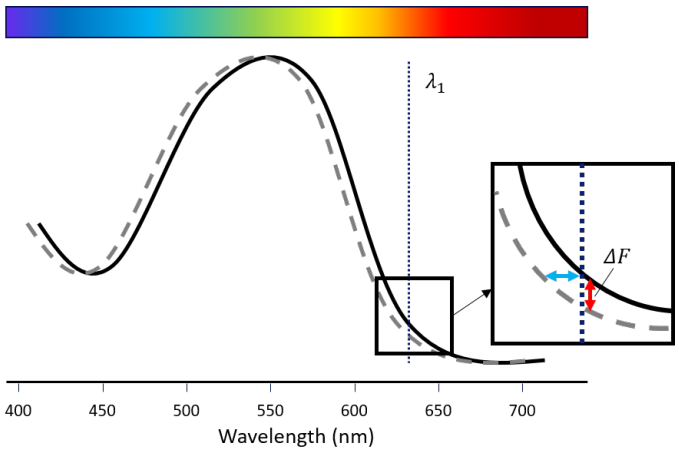

FIGURE 2.8: Spectral shift in a VSD. The black line shows the spectrum during the resting phase, the dashed grey line represents the spectral shift during depolarization. The blue dotted line shows the excitation at red (λ_1) light. The vertical displacement between the black and grey line (also indicated by the red arrow in the enlarged pane) is the ΔF. The blue arrow in the enlarged pane shows the voltage-dependent shift in absorbance.

Calcium indicators are used to study intracellular calcium handling. Calcium indicators consist of a chelator that binds to Ca^{2+}-ion, a fluorophore, and an ester to neutralize the charge. Calcium indicators enter the cytosol [59]. Within the cytosol, the chelator will bind with free calcium ions. Upon binding to a calcium ion, the fluorescence intensity of the calcium indicator is greatly increased. [61, 82,

83] Increases in cytosolic calcium concentration, for example, caused by CIRC, can be visualized using this mechanism. The calcium indicators have slower fluorescence kinetics compared to VSDs.

One of the main drawbacks of using calcium indicators is the high intensity of excitation light that is required. Most (ratiometric) calcium indicators are excited at wavelengths < 400 *nm* [84]. In the ultraviolet (UV) range of light, light intensities required for imaging can cause photodynamic damage to the tissue through the generation of reactive oxygen species (ROS) [61, 85, 86]. Photodynamic damage through ROS can alter the resting membrane potential, AP duration, and formation of afterdepolarization, and it can cause cellular inexcitability [85].

2.4 Artefact Reduction

Rather than preventing (motion) artefacts by immobilizing LMS, a combination of post-processing techniques can be used to correct the artefacts. Several methods are available to reduce the presence of artefacts in optical mapping. For this thesis, the focus is placed on image registration and ratiometry.

2.4.1 Image Registration

With image registration, a digital sequence of recordings can be spatially aligned. The aim of the alignment is that each recorded pixel represents an intensity measurement of the same tissue location over time. Usually, one image is the *set* or *fixed* image, and the other images are spatially transformed to fit the *fixed* image. The images that are being transformed are the *moving* images. Looking at *Figure* 2.6, this would mean that pixel *B*, during contraction, is registered to fit the location of pixel *A* during relaxation. Image registration can be feature- or intensity-based. In feature-based registration, local landmarks and edge detection, or foreign objects such as markers, are used to align images [87–89]. Intensity-based methods use similarities in the intensity levels of both images [90, 91].

There are four types of transformation [92]: rigid, affine, projective, and elastic (see *Figure* 2.9). The most robust form of image registration is rigid registration, where an image is merely translated and rotated. Affine registrations also allow shearing of the image. Projective registration maps lines to lines. The most complex form of image registration is called elastic or curved registration. Here, portions of an image can be warped or deformed.

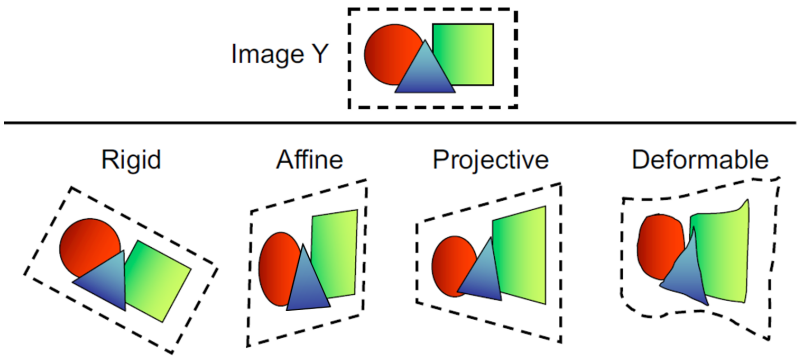

FIGURE 2.9: Example of registration methods, from [93].

2.4.2 Ratiometric Imaging

In addition to showing a spectral shift due to changes in V_m, some fluorophores display a change in fluorescence based on a shift in either the excitation or emission wavelength. This mechanism can be used for ratiometric imaging. An article by Zhang *et al.* [30] explains the mathematical relationship between the recorded fluorescence intensity and the V_m.

Ratiometric imaging is a method to reduce artefacts, which is performed with either multiple excitation [28] or emission [94] wavelengths. Here, the focus will be on excitation ratiometry. In excitation ratiometry, a fluorophore is alternately excited by two different excitation wavelengths, and a single emission band is recorded [28].

The theory behind ratiometric imaging is that the intensity-based changes in fluorescence vary upon excitation with different wavelengths, whereas ΔF due to artefacts remains constant. When the intensity ratio between two successive images is taken, the artefacts cancel each other out [94]. *Figure* 2.10 from [95] explains the principle of excitation ratiometry.

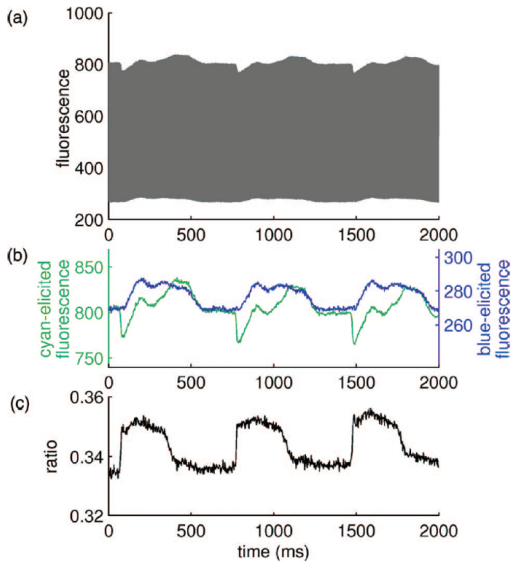

FIGURE 2.10: Excitation ratiometry example from [95]. (a) Time-interlaced fluorescence signal from a single region of interest. (b) De-interlaced signals, corresponding to alternating frames of cyan and royal blue excitation light. (c) Common artefacts in the two fluorescence signals are attenuated in the calculated ratio. Fluorescence units are analogue-to-digital conversion counts.

Design Considerations 3

In this proof of principle study, optical mapping of isotonically contracting LMS is performed. Until now, optical mapping has been performed on LMS in a limited number of studies. Each of these studies has used electromechanical uncoupling or suppression of contraction in some form. This is the first study in which optical mapping is performed in contracting LMS. Knowledge from Langendorff-perfused heart studies and electromechanically uncoupled LMS is translated to assemble an optical mapping system suitable for optical mapping isotonically contracting LMS. This chapter elaborates on the design considerations for such an experimental system.

As discussed in *Chapter* 2, an optical mapping system consists of a specimen, a fluorophore, a light source for excitation, a lens and emission filter to collect the emitted fluorescence, and a photodetector or camera to record the emitted fluorescence. The requirements and assumptions on which the selected materials are based are discussed below. One of the major considerations for assembling the optical mapping system is the possibility of adjusting the system from imaging LMS to a system suitable for future optical mapping experiments on *ex vivo* Langendorff-perfused hearts for future research.

3.1 Camera

The main requirement for an optical mapping system for LMS is the ability to record the rapid upstroke of the AP. The camera has to reach a frame rate of at least 2000 fps with a field of view (FOV) of approximately 15×15 *mm*. The FOV is based on the size of the LMS, including plastic triangles that are used to suspend the LMS in their BMCCs. Landmarks on the plastic suspenders can be used as landmarks for affine image registration. The frame rate of 2000 fps is based on the shape of the cardiac AP (see *Figure* 2.3). The duration of the rapid AP upstroke is 1-3 *ms*. According to the Nyquist sampling theorem, a frame rate of 1000 fps should be sufficient to record the shape of a rapid AP upstroke of 2 *ms* and, therefore, be able to discern the complete shape of the cardiac AP. However, with the use of ratiometric imaging for motion and artefact correction, half of the temporal resolution will be lost due to averaging of two consecutive images. An initial frame rate of 2000 fps will result in a corrected frame rate of 1000 fps after ratiometric artefact correction is performed. In theory, 2000 fps should suffice to visualize the rapid upstroke of the optical AP (OAP).

TABLE 3.1: Camera Specifications

Camera	**Frame Rate** (max. fps)	**Resolution*** (pixels)	**Pixel Size***	**Cost**	**QE** (at 700 *nm*)
KINETIX	$>$ 2000	1600×780	13×13 µm	$29,000	85 %
Mi-CAM Ultima	10,000	100×100	100×100 µm	$100,000	45 %
EVOLVE:128+	$>$ 2000	16×16	48×48 µm	$40,000	90 %
UI-3360CP-NIR-GL Rev.2	900	160×220	22×22 µm	$1,000	50 %
UI-3220CP-M-GL	400	160×220	24×24 µm	$700	50 %

*Resolution and pixel size after digital pixel binning

Most published studies either make use of fast, expensive cameras, such as the MiCAM ULTIMA-L system (100×100 pixels, 10,000 fps, $100,000), or slower, low-cost cameras (160×220 pixels, 400 fps, $700). See *Table* 3.1 for the specifications of often-used cameras. The frame rate of slower cameras can be increased to 1000 fps. However, this comes at the cost of a reduced resolution and FOV. As the frame rate of 2000 fps is a hard criterion, a broad range of low-cost cameras is not eligible.

The KINETIX (Teledyne Photometrix, Teledyne Scientific Imaging GmbH, Krailing, Germany) is a high-speed CMOS camera capable of reaching framerates of 5000 fps with a resolution 3200×320 pixels and 4×4 pixel binning. At lower framerates, even higher resolutions can be reached. The camera has a sensor array of 3200×3200 pixels (6.5×6.5 μm), and a peak quantum efficiency of 95%. Although this camera is ordinarily used for microscopic applications, a broad range of camera lenses can be mounted directly onto the camera, making it suitable for high-speed imaging of LMS.

3.2 Fluorophores

To maintain viable LMS, fluorophores that are excited by long wavelengths are preferred. Ratiometric calcium dyes are usually excited at wavelengths $<$ 400 nm, whereas ratiometric VSDs can be excited at longer wavelengths. Excitation at longer wavelengths reduces the risk of ROS production [61, 85, 96], therewith reducing the risk of AP alterations through excitation. Hence, for this proof-of-principle, VSDs are the preferred fluorophore. Furthermore, newer VSDs can be used for experiments in LMS as well as on Langendorff perfused hearts [96]. This would be beneficial for future extensions of the experimental setup. *Table* 3.2 gives a short summary of the different characteristics of voltage-sensitive and calcium dyes.

TABLE 3.2: Summary of voltage-sensitive and calcium dyes

Dye	**VSD/Calcium**	**Wavelength** (peak excitation, *nm*)	**Ratiometric**
Di-4-ANBDQBS	VSD	531	yes
Di-4-ANEPPS	VSD	470	yes
Di-4-ANBDQPQ	VSD	541	yes
RH237	VSD	550	no
Quin-2	Calcium	339	no
Rhod-2, AM	Calcium	552	no
Fura-2, AM	Calcium	335	yes
Fura-8	Calcium	355	yes
Fura-red	Calcium	435	yes

The VSD *di-4-ANBDQBS* (CytoVolt1, CytoCybernetics, Tonawanda, NY) is used. This is a ratiometric VSD that can be excited at long, red-shifted wavelengths and has been shown to be suitable for optical mapping on LMS and Langendorff-perfused heart preparations [96]. Di-4-ANBDQBQ has a $\Delta F/F_{max}$ of 15 to 20%, QY of 0.3, excitation/emission shift > 190 nm, and is non-toxic. Excitation ratiometry can be performed by exciting di-4-ANBDQBS at wavelengths of 480 nm (λ_{480}, blue light) and 640 nm (λ_{640}, red light) [97].

3.3 Optics

Light-emitting diodes (LEDs) are the preferred source of illumination. Compared to Tungsten-Halogen lamps, Mercury/Xeon arc lamps, and lasers, LEDs offer low heat generation, stable illumination, and can be switched on and off with rapid response times [77, 98]. Narrow ranges of excitation wavelengths can be achieved by placing filters in the path of the excitation light. Likewise, narrow bands of emission light can be captured by placing a filter in the optical path from the LMS to the photodetector.

For ratiometric imaging with di-4-ANBDQBS, excitation wavelengths of 480 nm and 640 nm are suitable. The two wavelengths are on either side of the peak excitation wavelength. Excitation at 480 nm shows a positive ΔF, linear to the increase in V_m, whereas excitation at 640 nm results in a negative ΔF, linear to the increase in V_m.

The emitted light is collected by a lens. A wide range of lenses is applicable to the KINETIX camera due to its swappable lens interface, allowing C-, F-, and T-mount lenses. The main considerations for a suitable lens are an appropriate FOV and working distance.

Before the light is collected by a lens, it is filtered. Di-4-ANBDQBS has an emission peak wavelength > 700 nm. Therefore, a long-pass filter > 700 nm or a band-pass filter near 700 nm should be used to filter the emission light.

3.4 Culture Conditions

To maintain viable LMS during optical mapping, optical mapping should be performed under cell culture conditions. The surrounding temperature should be 37°C, with 5% CO_2 concentration and saturating humidity.

Currently, optical mapping of cardiac slices has been performed in baths superfused with Tyrode's buffer, bicarbonate buffer, or Krebs solution. Culture medium containing Medium 199 (PAA Laboratories GmbHm, Austria) has the advantage of providing the tissue with nutrients and growth factors during experimenting.

In the case of this proof-of-principle, a pacing plate with BMCCs is transferred to the optical mapping system. LMS can be continuously paced on the chamber plate, and contractions can be measured in real-time. The plate enables rocking, which prevents the deposition of nutrients in the tissue medium. When images are acquired, the rocking is temporarily turned off.

Experimental Setup 4

In this chapter, the materials and methods for optical mapping on isotonically contracting LMS are discussed. First, the materials for the complete experimental setup are discussed, followed by the framework for motion correction and ratiometry. Next, the preparation of LMS and the optical mapping procedure are discussed.

4.1 System Design

The ratiometric VSD, di-4-ANBDQBS (CytoCybernetics, Tonawanda, NY), was used for the visualisation of the OAP in LMS. For ratiometric imaging, an illumination system (pE-300^{ultra}, CoolLED, Andover, United Kingdom) with three LED sources was implemented. Two bandpass excitation filters, at 480 *nm* (ET480/20x, FWHM 20 *nm*, Chroma Technology GmbH, Olching, Germany) and 640 *nm* (ET640/20m, FWHM 20 *nm*, Chroma Technology GmbH, Olching, Germany), were inserted. A C-series Voltage Output Module (NI-9263, National Instruments, Austin, Texas, USA), in combination with a chassis (cDAQ-9171, National Instruments, Austin, Texas, USA), was used to synchronize the LED excitation with the camera frame rate through a script in MATLAB 2022b (see *Appendix* A.1) (MathWorks Inc., USA). The emission light passed through a 705 *nm* bandpass filter (AT705/30m, 705 *nm*, FWHM 30 *nm*, Chroma Technology GmbH, Olching, Germany) and was collected by a 1× magnifying lens (CS12ZA-1S, Vision Light Tech B.V., Uden, The Netherlands). Fluorescence images were taken by a high-speed CMOS camera (KINETIX, 3200×3200 pixels, Teledyne Photometrics, Teledyne Scientific Imaging GmbH, Krailing, Germany) at 2000 fps. Image acquisition was performed with the open-source Micro-Manager software (Vale Lab, University of California, San Francisco, USA) [99].

Image Acquisition Settings

Before proof-of-principle experiments were performed, image acquisition settings were determined. Based on camera the requirement to reach 2000 fps, settings were determined for FOV, pixel binning, and illumination intensity. The intensity of the blue and red excitation light was scaled to achieve equal illumination intensity at both wavelengths. Images were visually inspected before preprocessing.

Motion correction

To perform motion correction, four markers were placed on the plastic triangles attached to the LMS (see *Figure* 5.9). These markers were opaque, which hindered the emittance of fluorescent light from the tissue underneath these markers. The markers functioned as reference points for image registration.

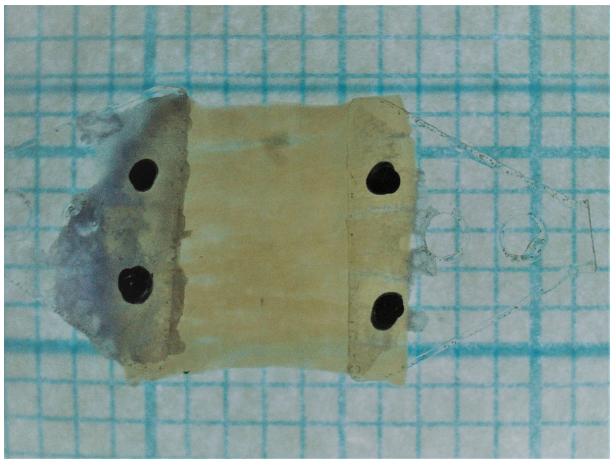

FIGURE 4.1: LMS with opaque markers placed on the plastic suspension triangles

Ratiometric Imaging

To perform ratiometric imaging, the camera frame rate and LED illumination interval had to be synchronized. The camera and the illumination system were synchronized by intermittently sending 5 V transistor-transistor logic (TTL) pulses to the blue and red LED channels in the pE-300^{ultra}, and simultaneously sending a 5 V TTL pulse to the camera (see *Figure* 4.2). These TTL pulses were programmed in MATLAB (see *Appendix* A.1), and sent to the illumination system and the camera via a voltage output module (NI 9263, C-Series Voltage Output Module, National Instruments, Austin, Texas, USA).

4.2 LMS preparation

Experiments were performed on human left ventricular LMS. LMS were prepared according to the slicing protocol by Amesz and Taverne [100]. The LMS were cultured in culture medium (Medium 199, 1% penicillin/streptomycin (PAA, Austria), ITS supplement (Sigma-Aldrich, USA, composition: insulin 10 mg/L, transferrin 5.5 mg/L, and selenium 5 $\mu g/L$)) in BMCCs. The LMS were mechanically stretched to obtain a preload of 1.2 mN and were paced at 0.5 Hz. Pacing and contractile force measurements were performed with the MyoDish software [18].

4.2.1 Fluorophore loading

LMS were loaded with 2.4 ml of 42 μM Di-4-ANBDQBS (100 $nmol$ Di-4-ANBDQBS dissolved in 10 μl 100% ethanol, diluted in 2.39 ml culture medium). The fluorophore was incubated in the LMS for 30 minutes under continuous pacing at 0.5 Hz. After dye loading, the dye solution was replaced with fresh culture medium. See *Appendix* B.1 for a step-by-step description of the fluorophore preparation and loading.

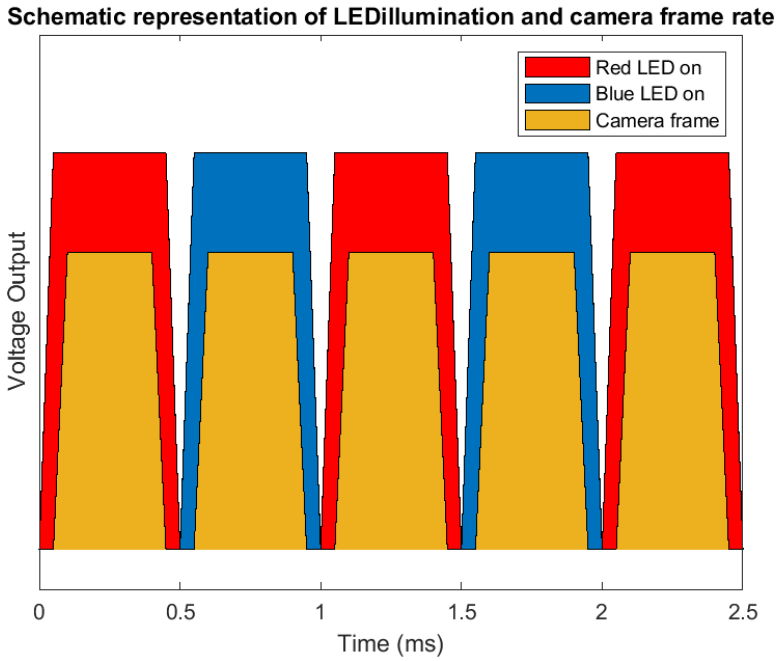

FIGURE 4.2: Schematic representation of TTL-pulse train for LED and camera output. Voltage output is not to scale.

4.3 Optical Mapping

The culture dish was placed directly under the camera lens (see *Figure* 4.3). The camera was focused and aligned. The blue channel, λ_{480}, and the red channel, λ_{640}, of the illumination system were used to excite the fluorophore. The channels were switched on intermittently for ratiometric imaging. Pacing was continued at 1 *Hz*. 2-second optical mapping recordings were acquired. Contractile force was measured continuously using MyoDish (InVitroSys GmbH, Gräfelfing, Germany). See *Appendix* B.2 for a detailed, step-by-step description of the experimental protocol.

4.3.1 Preprocessing

Before analysis could be performed, multiple steps in data processing were required. These steps were performed in MATLAB 2022b (see Appendix A). First, the intensity of the frames was scaled to increase the contrast between the LMS and the background. Second, a disk-shaped two-dimensional (2D) filter ($r = 3$ pixels) was applied to smooth the frames (see *Appendix* A.2). The markers for motion correction were segmented. A robust motion correction was performed, based on affine registration of the markers with SimpleElastix (Stefan Klein & Marius Staring, Image Sciences Institute, University Medical Center Utrecht, the Netherlands) [101, 102]. Next, a rectangular region of the LMS was segmented. Hereafter, ratiometric correction was performed for noise removal (see *Appendix* A.3). The ratio was taken by calculating the average of two subsequent red-illuminated images and dividing the average by its intermediate blue-illuminated image:

$$I_{ratio}(t) = \frac{I_{\lambda_{640}}(t-1) + I_{\lambda_{640}}(t-1)}{2} / I_{\lambda_{480}}(t) \; . \tag{4.1}$$

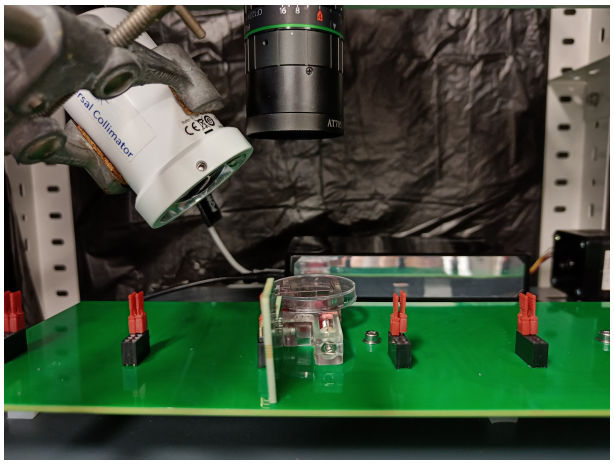

FIGURE 4.3: Placement of LMS culture chamber underneath camera lens

Performing the ratiometric correction would result in a data set with half the number of frames of the original data set.

4.3.2 Data Analysis

Data analysis was performed using the open-source software ElectroMap [79]. The software generated a graph of the fluorescence intensity over time, representing the averaged AP morphology. Mean values for AP duration at 90% repolarisation (APD_{90}), CV, amplitude, and SNR were calculated. APD_{90} maps, activation maps, and SNR maps could be generated.

Results 5

This chapter contains the results of the system design. After the system design, the chapter continues to preliminary results of optical mapping preprocessing and data analysis. Finally, the results of a proof of principle experiment are presented.

5.1 System Design

A fully operational optical mapping system (see *Figure* 5.1), including the ability to pace LMS and measure isotonic contraction force, was built. The system could be warmed up to 37°C, simulating physiological temperatures for the environment. Through a comprehensive manual (*Appendix* B), members of the *translational electrophysiology department* were able to perform optical mapping experiments with the optical mapping system.

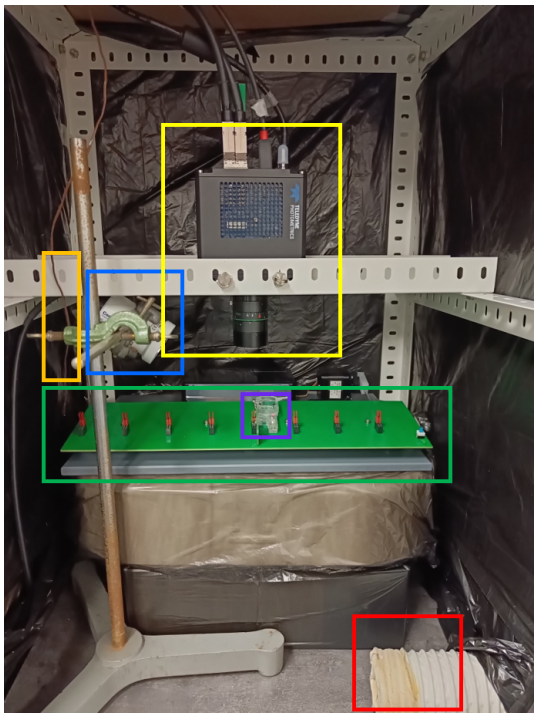

FIGURE 5.1: Optical mapping system, camera and lens (yellow box) including pacing plate (green box), BMCC (purple box), LED collimator (blue box), thermocouple (orange box), and temperature control (red box)

Dye excitation was enabled through a pE-300^{ultra} illumination system (CoolLED, Andover, United Kingdom). A 480 *nm* filter (ET480/20x, FWHM 20 *nm*, Chroma Technology GmbH, Olching, Germany) with a FWHM of 20 *nm* and a 640 *nm* filter (ET640/20m, FWHM 20 *nm*, Chroma Technology GmbH, Olching, Germany) with a 20 *nm* FWHM were inserted into the illumination system. The filtered light was guided to the LMS through a liquid light guide and a universal collimator. For blue-light illumination, no light below 465 *nm* and no light above 495 *nm* could pass the filter. No light below 625 *nm* and above 655 *nm* could pass the red light filter.

It was possible to alternately illuminate a LMS at (λ_{480}) and (λ_{640}) (see *Figure* 5.2a and 5.2b) at 2000 Hz. For image acquisition, the FOV was set to 130×130 pixels (2×2 pixel binning), and the exposure time was set to 0.35 *ms*

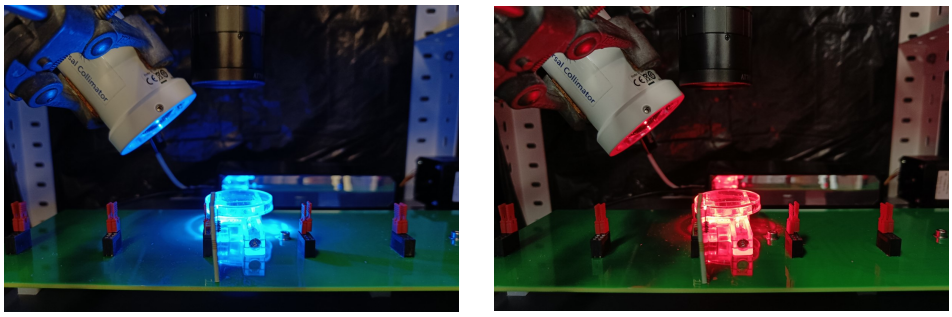

(A) LMS illumination at 480 *nm* (B) LMS illumination at 640 *nm*

FIGURE 5.2: Blue (A) and red (B) light illumination

Image Acquisition Settings

The relative irradiance of the excitation light sources differed. CoolLED gave a rough estimation of the relative irradiance for the lightspectrum of the pE-300^{ultra}. The transmission spectra from the excitation filters were both roughly rectangle-shaped. Based on these spectra, an average relative irradiance was calculated. *Figure* 5.3 gives a visual representation of the bandwidth which is allowed to pass the excitation filters. As it was stated by *Chroma Technology* that transmission spectra could vary from lot to lot, it was assumed that the transmission curve for the two filters was block-shaped with a transmission of 97% over the whole FWHM. This resulted in the following illumination intensities:

$$I_{\lambda_{480}} = \frac{0.2800 + 0.0002}{2} * 0.97 = 0.136 \tag{5.1}$$

$$I_{\lambda_{640}} = \frac{0.1300 + 0.0875}{2} * 0.97 = 0.105 \tag{5.2}$$

which translates to a 33% higher relative irradiance for blue-light excitation. Therefore, the blue excitation light was set to 67% illumination intensity.

Initial image acquisition settings were determined, based on visual inspection, the ability to segment the LMS, and reaching a frame rate of 2000 fps. At a FOV of 3200×800 pixels (2×2 pixel binning), a frame rate of 1992 fps could be reached. By decreasing the FOV further, speeds over 2000 fps could be reached. A FOV of 130×130 pixels (2×2 pixel binning) was suitable for reaching frame rates $>$ 2000

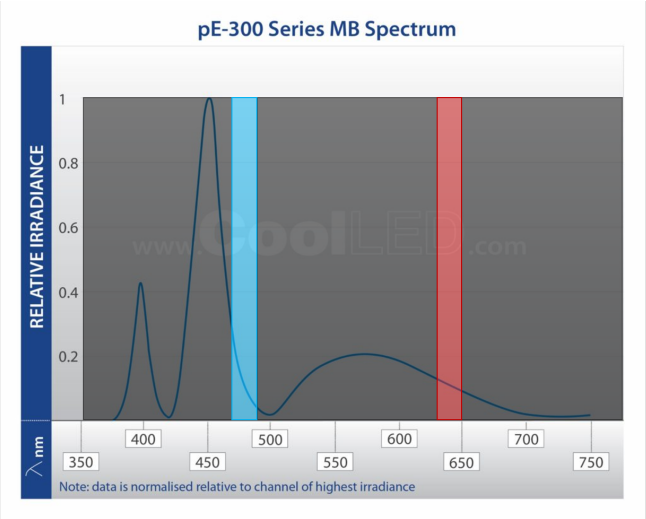

FIGURE 5.3: Relative irradiance of pE-300^{ultra}, with excitation bandpass filters visualised in blue and red.
Edited figure from CoolLED [103]

fps during ratiometric imaging and was adequate to record the complete LMS and markers.

The exposure time was set to 0.35 *ms* in the Micro-Manager graphical user interface. This ensured a frame rate of 2000 fps during ratiometric imaging. The exposure time could be set to 0.49 *ms* at single wavelength imaging.

Ratiometric Imaging

Three separate TTL voltage outputs were programmed to control the blue LED channel, red LED channel, and camera. At $t = 0$ *ms*, the camera was activated by a train of TTL pulses. After 30 seconds, a stable frame rate of 2000 fps was reached. Every 0.5 *ms*, the camera was switched on for 0.4 *ms*. After reaching a steady frame rate, the blue LED channel was intermittently switched on and off for 0.5 *ms*. Interleaved with the blue LED channel, the red LED channel was switched on and off with 0.5 *ms* time intervals. The camera exposure time of 0.35 *ms* ensured that the camera only recorded a frame during full-intensity illumination of the LEDs.

5.2 Optical Mapping

Optical mapping experiments were performed on a human left ventricular LMS. Pacing was set to 1 Hz and the frame rate was set to 2000 fps, ensuring the recording of a whole contraction. Simultaneously with the optical mapping recording, the contractile force of the LMS was measured in the BMCC. Each recording resulted in a *.tiff* file with 4000 frames, consisting of 2000 blue-illuminated frames and 2000 red-illuminated frames. *Figure* 5.4 shows an example of the raw output data. Alongside optical mapping recordings, MyoDish was used to perform contractile force measurements (see *Figure* 5.5). This LMS exerted a force of nearly 1000 *mN* during contraction.

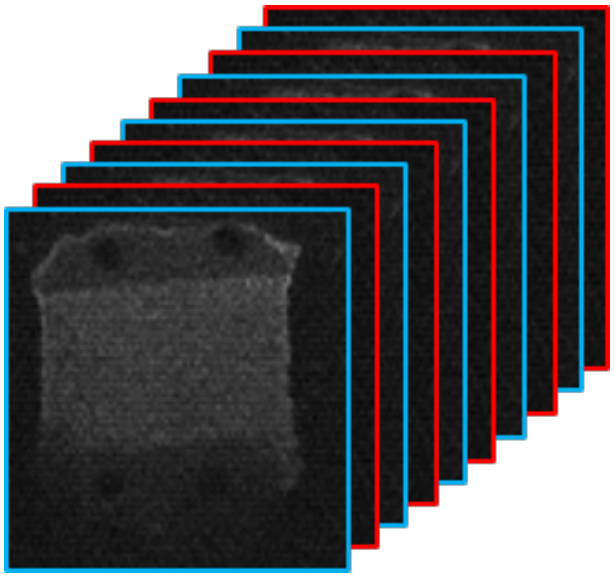

(A) Schematic representation of an optical mapping image array

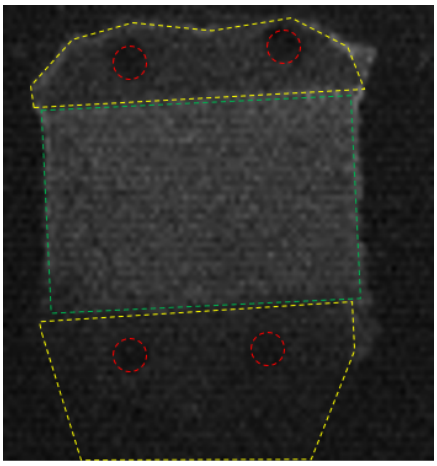

(B) Frame of a recording of a LMS with markers, illuminated with blue light

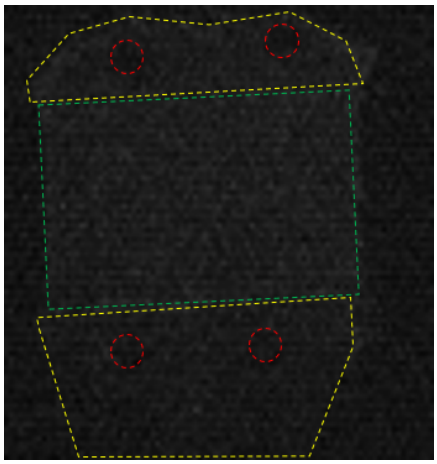

(C) Frame of a recording of a LMS with markers, illuminated with red light

FIGURE 5.4: Unprocessed frames of a ratiometric optical mapping recording of a LMS, with a 705 *nm* band-pass filter. (A) Shows an image array of 10 consecutively recorded frames, the blue and red borders are indicating the illumination with either blue or red light. (B) Shows the first frame of a recording, illuminated with blue light. (C) Shows the first frame of the same recording, illuminated with red light. In (B) and (C) the red-dashed areas indicate the markers, the green-dashed area is the viable portion of the LMS, and the yellow-dashed areas represent tissue glued to the plastic triangles.

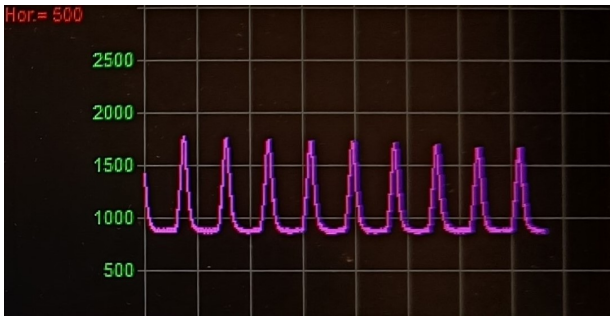

FIGURE 5.5: Screencapture of a contractile force measurement during optical mapping. The purple line shows the force that is generated by the LMS, in *mN* during contraction

5.2.1 Preprocessing

The markers were segmented for motion correction (see *Figure* 5.6a and 5.6b). Based on the marker segmentation, image registration was performed. All the frames were registered to the first frame. After image registration, ratiometric correction was performed to further reduce (motion) artefacts. According to *Equation* 4.1, the ratio of the average of two red-illuminated frames and the intermediate blue-illuminated frames of a segment of the LMS was taken. *Figure* 5.7 shows a plot of the pixel intensity of a single pixel over time for the blue-illuminated frames, the averaged red-illuminated frames, and in the next window, the resultant pixel intensity after ratiometric correction.

5.2.2 Data Analysis

After motion correction, data analysis of a segmented section of the LMS was performed using ElectroMap. *Figure* 5.8 shows a graph of the total fluorescence intensity over time. When peak distance was set to a minimum peak distance of 700 *ms*, the blue highlighted portion of the signal was distinguished as a repetitive

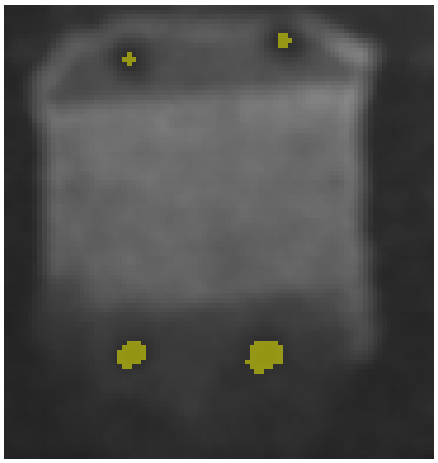

(A) LMS after preprocessing, illuminated with blue light

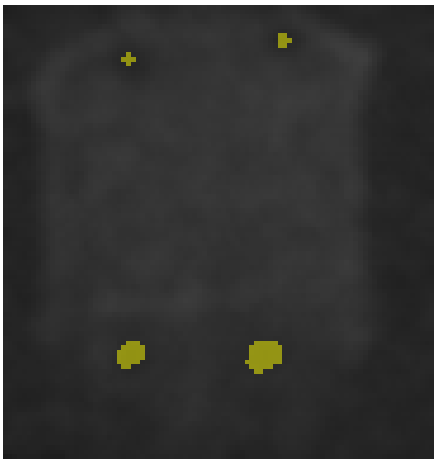

(B) LMS after preprocessing, illuminated with red light

FIGURE 5.6: Result of the first blue-illuminated (A) and red-illuminated (B) preprocessed frames of a LMS, acquired with ratiometric optical mapping, with a 705 *nm* band-pass filter. Marker segmentation is shown in yellow

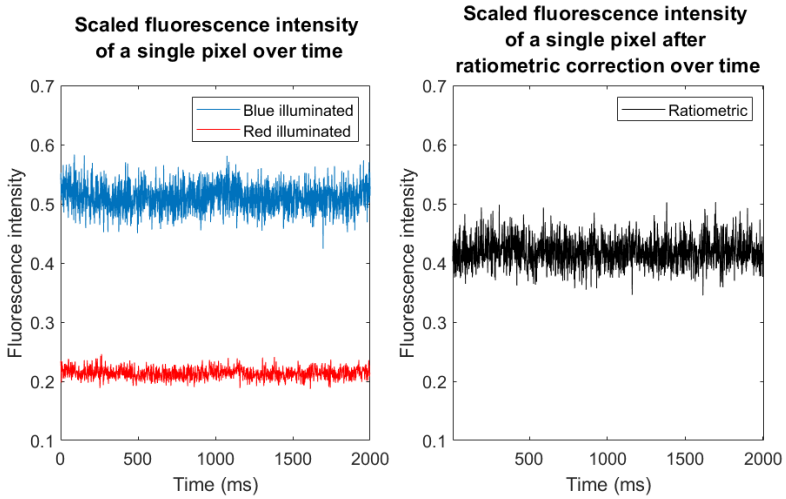

FIGURE 5.7: Fluorescence intensity over time for a single pixel. The first panel shows the pixel intensity for a pixel in blue- and (averaged) red-illuminated frames. The second panel shows the pixel intensity for the same pixel after ratiometric correction.

frequency. A cycle length of 886 *ms* was estimated. This is less than 1*s*, which was the expected cycle length, as pacing was set to 1 *Hz*. Distinctive AP characteristics, such as the rapid upstroke and plateau phase were not present.

An APD_{90} map (see *Figure* 5.9a), activation map (see *Figure* 5.9b), and SNR map (see *Figure* 5.9c) were generated. The APD_{90} and activation maps do not show any distinctive patterns. The SNR map shows a relatively low SNR throughout the LMS. According to ElectroMap, the total activation time was 69.8617 *ms*, the mean APD_{90} was 11.9167 *ms* (SD = 8.4422), the mean CV was 0.5688 *ms* (SD = 0.3470). These values are low, compared to normal values for APD and CV, known from literature.

TABLE 5.1: ElectroMap Output

	Mean	**SD**	**Variance**
APD_{90} (*ms*)	11.9167	8.4422	71.2715
CV (*cm/s*)	0.5688	0.3470	0.1204
SNR	2.5070	7.8443	0.2110

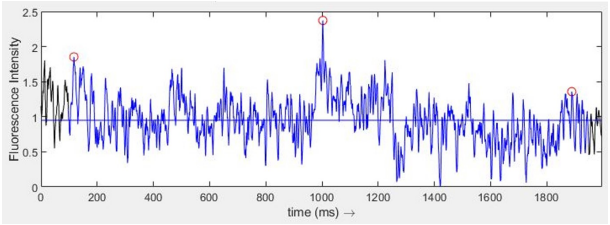

FIGURE 5.8: Screencapture of the graphed fluorescence intensity (arbitrary units) over time, from ElectroMap. The blue segment is recognized as a repetitive frequency with a cycle length of 886 *ms* (1.1236 *Hz*). The red dots represent the peaks on which the cycle length is based.

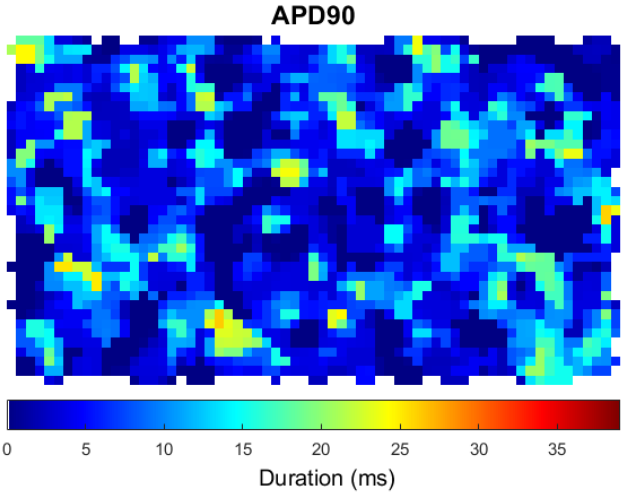

(A) APD map of a LMS segmentation, after 90% repolarization. The different colours represent the averaged time it took the sum of cells in each pixel to reach 90% repolarization after the start of the AP

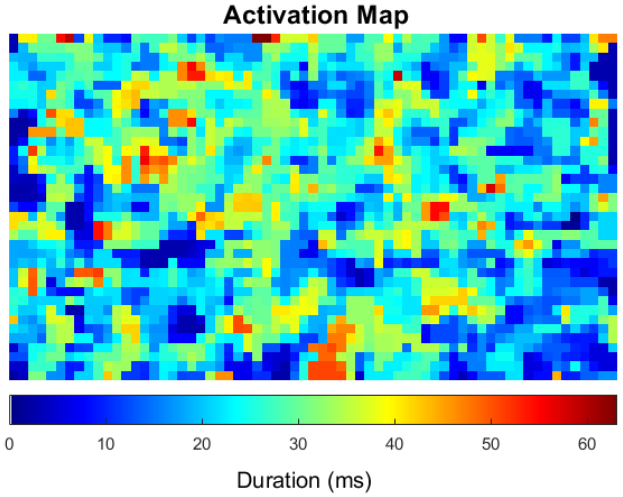

(B) Activation map of a LMS segmentation. The colours represents the time between activation of the first (dark blue) and last regions (dark red)

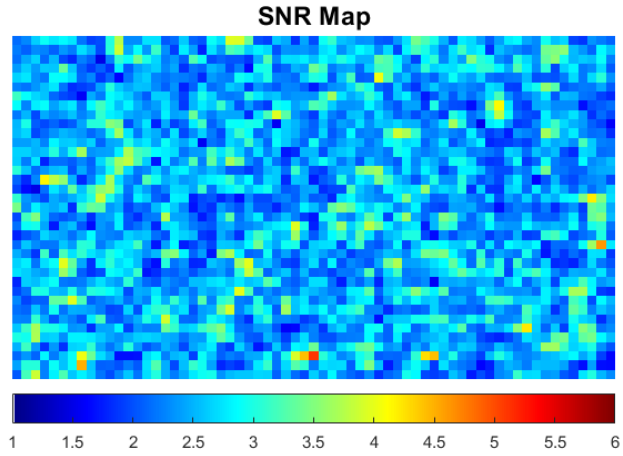

(C) SNR map of a LMS segmentation

FIGURE 5.9: Maps for APD_{90}, activation, and SNR of a segmentation of a LMS

6 Discussion

This thesis aimed to set up an optical mapping system and to perform, to my knowledge, the first (proof-of-principle) optical mapping experiments on isotonically contracting LMS.

A fully operational optical mapping system was built. This optical mapping system could reach frame rates of over 2000 fps, making it suitable for recording the rapid upstroke of the cardiac AP. First steps were taken in correcting motion artefacts from the contracting LMS by performing image registration and ratiometric imaging. To my knowledge, this is the first optical mapping system that is used to study electromechanically coupled LMS. It was possible to record APs while simultaneously measuring the force of the isotonic contractions of LMS, enabling the next steps in unravelling the mechanisms of excitation-contraction coupling in cardiac tissue.

6.1 Experimental Setup

Since optical mapping made its entrance into cardiac electrophysiological research, many steps have been taken to improve the technique. There has been a debate on the influence of pharmacological uncouplers on AP morphology. However, there is increasing evidence that uncouplers can alter the electrophysiologic behaviour of the LMS [26, 27]. Additionally, uncoupled tissue has reduced oxygen consumption [104], and, more importantly, electromechanical uncoupling prevents studying the ECC mechanism. In this thesis, no pharmacological uncouplers were used, meaning that the AP was not altered. This results in an *in vitro* model with a better *in vivo* representation compared to other current *in vitro* models. Furthermore, the BMCCs allow isotonic force measurements alongside electrophysiological measurements.

Most knowledge on cardiac optical mapping in contracting tissue is gained from Langendorff-perfused heart studies. Compared to Langendorff-perfused hearts, optical mapping of LMS has the potential for a far greater temporal resolution. Optical mapping of thick tissues results in elongated OAPs. Optical mapping of LMS is better capable of following the rapid upstroke of the AP. However, it should be noted that the OAP is a summation of the fluorescence captured by each pixel. A pixel contains the weighted sum of every single-cell V_m in a pixel volume (voxel) [67, 105]. In comparison, electrode mapping detects the electrical signals in close vicinity of the electrodes [106]. The most commonly used multi-electrode array (MEA) has electrodes with a diameter of 30 μm and an inter-electrode distance of 200 μm. However, MEAs do not allow simultaneous isotonic force measurements

since the tissue is pressed against the electrode. Hence, optical mapping is superior when it comes to investigating ECC.

Most optical mapping studies make use of a relatively low temporal resolution. An article on building a low-cost optical mapping system in translational heart models by Lee *et al*. [107] made the assumption that a sampling frequency of 300 *Hz* would be sufficient to visualize the OAP. Their assumptions were based on previous studies that showed negligible signal content above 100 *Hz* in porcine hearts [36]. In thick tissue, fluorescence originates from deep layers of muscle tissue as well as superficial layers. Studies have shown that ranges from 300 to 500 *µm* [66, 67] and ranges up to 2 *mm* [68] can contribute to the fluorescence signal. The contribution of fluorescence from deep tissue layers (2 *mm*) results in an increased AP upstroke duration: from 1 to 2 *ms* to 13 *ms* or more due to scattering and fluorescence from outside the FOV [105]. Due to the thin nature of LMS, no scattering of fluorescence from deep tissue layers can occur. It can be presumed that the OAP of LMS closely follows the electrical AP due to their thin nature and absence of scatter from outside the FOV, hence showing a rapid upstroke phase in the OAP. Therefore, the optical mapping system presented in this thesis required a much higher frame rate compared to Langendorff-perfused heart optical mapping studies. The high temporal resolution will allow a much more detailed investigation of the cardiac AP and the tissue's response to pharmacological agents compared to Langendorff-perfused heart studies.

Multiple system configurations were possible for the optical mapping system. A major consideration in system configuration is the use of a single or dual-camera design. The advantage of a dual-camera design is that multiple probes can be recorded simultaneously by applying different emission filters to the cameras. Tissue can be constantly illuminated with a single light source. Similarly, ratiometric imaging can be performed by constant illumination with a single light source, and emission light can be captured in two differing emission bands, known as emission ratiometry. This would preclude complex synchronization problems which are encountered in excitation ratiometry. However, the camera is by far the most expensive component of the optical mapping system. Using two cameras rather than one would nearly double the cost of building such a system. A single-camera design is more cost-efficient. However, a single-camera configuration requires complex illumination sequences, which also require additional preprocessing steps. The sequential recording of images for ratiometry or multi-probe imaging also reduces the temporal resolution.

Combined with motion correction techniques, these considerations make for an ideal system in which electrophysiological parameters can be studied alongside isotonic force measurements in LMS.

6.2 Optical Mapping

This thesis presents the first experimental data of an optical mapping experiment on isotonically contracting LMS. Although motion correction was performed, based on image registration and ratiometry, the experimental results were ambiguous. *Figure* 5.8 does not show a clear AP shape, and the cycle length of 886 *ms* does not correspond to the pacing frequency of 1 *Hz*. Furthermore, the APD_{90} of 11.9 *ms* and CV of 0.5 *cm/s* are far too low for ventricular tissue. Normal APD and CV values would be around 300 *ms* and 2 *cm/s* in ventricular tissue, respectively.

The abnormal APD and CV measures might be explained by the method of stimulation. First, it is not know what effect field stimulation has on the ionic currents. It is possible that field stimulation leads to an abrupt opening of the slow calcium channels, rather than the opening of fast sodium channels and closing of potassium channels. This would result in an abnormal AP shape and duration. Furthermore, it is unclear what kind of CV should be expected in a field-stimulated tissue rather than a point-stimulated tissue. Similarly, it is not known what type of pattern could be expected in the activation map. While these parameters were not compared to any reference, a much higher CV would be a more likely outcome since it is assumed that the cells are nearly simultaneously excited. The simultaneous activation would presumably result in a CV which approaches infinity.

6.3 Strengths and Limitations

The greatest strength of the presented optical mapping system is that it enables the simultaneous investigation of AP conduction and contractility in LMS. The system is capable of reaching high frame rates with a relatively large FOV. The combination of marker-based image registration and ratiometry allows for a robust motion correction.

Currently, markers for image registration are placed on top of plastic triangles which are glued to the LMS (see *Figure* 5.9). The marker placement ensures that no relevant fluorescence signal is obscured. As could be seen in *Figure* 5.4, the fluorescence signal is decreased where plastic triangles are glued to the LMS (yellow-dashed areas). The area underneath the plastic triangles is not considered an area for investigation since cells that come in contact with histo-acryl undergo cell death. Furthermore, the current marker placement does not alter the electrophysiologic properties nor does it cause conduction blocks.

The current marker placement ensures that no relevant fluorescent signal is lost. Nonetheless, these markers are not a completely accurate representation of the motion of the LMS. Since the markers are placed on plastic triangles, the markers can solely undergo linear translation. The markers do not enable tracking of tissue deformation because they are placed on solid plastic triangles. The linear translation can be corrected with rigid or affine registration techniques. However, during image acquisition, non-homogeneous tissue deformation was seen. Thus far, no studies in which motion correction is performed on LMS, have been published. Presently, there are studies in which motion correction is performed on optically mapped Langendorff-perfused hearts [30, 104]. Assumptions made in these Langendorff-perfused heart studies were translated into this optical mapping system. Zhang *et al.* [30] made use of motion tracking based on circular markers in combination with ratiometry. They assumed that the tissue deformation within their ROI was homogeneous. In their study, a distance error < 1 pixel (24 x 24 μm) was seen between the measured and interpolated positions in an equilateral triangle with sides of 8 *mm* in length. They assumed that a length of up to 15 *mm* would give similar results. Based on these statements, the assumption was made that the deformation in the LMS model would also be homogeneous. Due to the non-homogeneous tissue deformation, seen in recordings, this assumption does not hold for LMS. Perhaps, the non-homogeneous tissue deformation in the LMS is caused by their thin nature and the helical orientation of cardiac cells. Other techniques, such as non-rigid image registration and optical flow [108] should be explored to improve motion correction.

The current optical mapping data does not show classic activation (see *Figures* 5.9b). This could be explained by shortcomings in motion correction. However, activation maps are deemed to look different based on the type of tissue stimulation. In a point-stimulated LMS, it is expected to see a wave pattern spreading out from the point of stimulation. In a field-stimulated LMS, every cell is expected to be depolarized nearly simultaneously. Nearly simultaneous stimulation of every cell is likely to result in activation maps without an obvious activation pattern. Therefore, a next step in improving the optical mapping system would be the implementation of point stimulation. This would allow the generation of more familiar activation maps to validate the current optical mapping system.

A remaining challenge is making a user-friendly framework for image acquisition. External software, such as the TTL-pulse programming and MyoDish software, should be combined with the image acquisition software.

Finally, LMS were mapped in BMCCs, placed in an optical mapping setup of 37°C. This ensured a relatively stable environment for the LMS. In this experimental optical mapping setup, O_2 and CO_2 concentrations, and humidity could not be controlled. A next advancement in the presented optical mapping system should be further stabilization of the desired environmental variables.

6.4 Future Perspective

The presented optical mapping system can be converted to a CaT imaging system. Both V_m and CaT-related research questions can be tackled using this unique system.

Currently, there is no literature stating the desired irradiance for fluorophore excitation. Furthermore, there is not yet a standardized method to measure irradiance [109]. Additionally, there is no standardized fluorophore concentration. Fluorophore concentrations vary among different dyes, types of tissue, and dye-loading protocols [110–113]. In this study, the fluorophore concentration of 42 μM is based on advice from the fluorophore producer. For future research it is interesting to find the optimal irradiance to minimalize illumination induced tissue damage, and the optimal fluorophore concentration for cost efficient V_m measurements.

Many mechanisms in HF are still unknown. With the combination of electrophyisiological examination, calcium imaging, and isotonic force measurements, it might become possible to find the underlying cause of HF. Tissues, obtained from different groups of patients, can be used to mimic the stages of HF to try and gain better understanding of the role that ECC plays in the development of HF.

Furthermore, different pacing sequences can be used to mimic or induce cardiac arrhythmias in the LMS. Optical mapping could aid in gaining a better understanding in the changes AP propagation and its relationship with changes in isotonic contractile force.

In the translational electrophysiology laboratorium, responses to different types of HF or anti-arrhythmia medication could be studied directly after tissue is obtained from a patient. Such short links between research and clinical practice can help in prescribing patient-tailored medication.

Finally, due to the unique setting, tissue obtained from cardiac surgery could be transferred to the electrophysiology lab to study AP conduction and calcium handling, after electrode measurements have been performed on the same tissue in the operation room. Potentially, this could help interpret the electrode measurements.

6.5 Conclusion

To conclude, this thesis presents a unique system for real-time simultaneous assessment of electrophysiological and mechanical parameters in LMS. With further improvements, this optical mapping system has the potential to become an invaluable tool in the investigation and treatment of cardiac arrhythmias and heart failure.

Bibliography

[1] Connie W. Tsao et al. "Heart Disease and Stroke Statistics—2022 Update: A Report From the American Heart Association". In: *Circulation* 145.8 (Feb. 2022), E153–E639. ISSN: 0009-7322. DOI: 10.1161/CIR.0000000000001052. URL: https://www.ahajournals.org/doi/10.1161/CIR.0000000000001052.

[2] Gary Tse. "Mechanisms of cardiac arrhythmias". In: *Journal of Arrhythmia* 32.2 (2016), pp. 75–81. ISSN: 18832148. DOI: 10.1016/j.joa.2015.11.003. URL: http://dx.doi.org/10.1016/j.joa.2015.11.003.

[3] Christopher O'Shea et al. "Cardiac optical mapping – State-of-the-art and future challenges". In: *International Journal of Biochemistry and Cell Biology* 126.May (2020), p. 105804. ISSN: 18785875. DOI: 10.1016/j.biocel.2020.105804. URL: https://doi.org/10.1016/j.biocel.2020.105804.

[4] Alec S.T. Smith et al. "Human iPSC-derived cardiomyocytes and tissue engineering strategies for disease modeling and drug screening". In: *Biotechnology Advances* 35.1 (Jan. 2017), pp. 77–94. ISSN: 07349750. DOI: 10.1016/j.biotechadv.2016.12.002. URL: https://linkinghub.elsevier.com/retrieve/pii/S0734975016301574.

[5] Thomas Eschenhagen et al. "Three-dimensional reconstitution of embryonic cardiomyocytes in a collagen matrix: a new heart muscle model system". In: *The FASEB Journal* 11.8 (July 1997), pp. 683–694. ISSN: 0892-6638. DOI: 10.1096/fasebj.11.8.9240969. URL: https://onlinelibrary.wiley.com/doi/abs/10.1096/fasebj.11.8.9240969.

[6] José M. Di Diego et al. "Optical and electrical recordings from isolated coronary-perfused ventricular wedge preparations". In: *Journal of Molecular and Cellular Cardiology* 54.1 (Jan. 2013), pp. 53–64. ISSN: 00222828. DOI: 10.1016/j.yjmcc.2012.10.017. URL: http://dx.doi.org/10.1016/j.yjmcc.2012.10.017%20https://linkinghub.elsevier.com/retrieve/pii/S0022282812003999.

[7] Robert M. Bell, Mihaela M. Mocanu, and Derek M. Yellon. "Retrograde heart perfusion: The Langendorff technique of isolated heart perfusion". In: *Journal of Molecular and Cellular Cardiology* 50.6 (June 2011), pp. 940–950. ISSN: 00222828. DOI: 10.1016/j.yjmcc.2011.02.018. URL: http://dx.doi.org/10.1016/j.yjmcc.2011.02.018%20https://linkinghub.elsevier.com/retrieve/pii/S0022282811000952.

[8] Matthew A. Schechter et al. "An Isolated Working Heart System for Large Animal Models". In: *Journal of Visualized Experiments* 88 (June 2014), pp. 4–11. ISSN: 1940-087X. DOI: 10.3791/51671. URL: http://www.jove.com/video/51671/an-isolated-working-heart-system-for-large-animal-models.

[9] J Mitcheson. "Cultured adult cardiac myocytes Future applications, culture methods, morphological and electrophysiological properties". In:

Cardiovascular Research 39.2 (Aug. 1998), pp. 280–300. ISSN: 00086363. DOI: 10.1016/S0008-6363(98)00128-X. URL: https://academic.oup.com/cardiovascres/article-lookup/doi/10.1016/S0008-6363(98)00128-X.

[10] Filippo Perbellini and Thomas Thum. "Living myocardial slices: a novel multicellular model for cardiac translational research". In: *European Heart Journal* 41.25 (July 2020), pp. 2405–2408. ISSN: 0195-668X. DOI: 10.1093/eurheartj/ehz779. URL: https://academic.oup.com/eurheartj/article/41/25/2405/5621351.

[11] C. Kang et al. "Human Organotypic Cultured Cardiac Slices: New Platform For High Throughput Preclinical Human Trials". In: *Scientific Reports* 6.1 (Sept. 2016), p. 28798. ISSN: 2045-2322. DOI: 10.1038/srep28798. URL: http://www.nature.com/articles/srep28798.

[12] Matthias Brandenburger et al. "Organotypic slice culture from human adult ventricular myocardium". In: *Cardiovascular Research* 93.1 (Jan. 2012), pp. 50–59. ISSN: 1755-3245. DOI: 10.1093/cvr/cvr259. URL: https://academic.oup.com/cardiovascres/article-lookup/doi/10.1093/cvr/cvr259.

[13] Fotios G. Pitoulis et al. "Myocardial slices come to age: An intermediate complexity in vitro cardiac model for translational research". In: *Cardiovascular Research* 116.7 (2020), pp. 1275–1287. ISSN: 17553245. DOI: 10.1093/CVR/CVZ341.

[14] Moustafa H. Meki, Jessica M. Miller, and Tamer M.A. Mohamed. "Heart Slices to Model Cardiac Physiology". In: *Frontiers in Pharmacology* 12.February (2021), pp. 1–8. ISSN: 16639812. DOI: 10.3389/fphar.2021.617922.

[15] Samuel A. Watson, Cesare M. Terracciano, and Filippo Perbellini. "Myocardial Slices: an Intermediate Complexity Platform for Translational Cardiovascular Research". In: *Cardiovascular Drugs and Therapy* 33.2 (Apr. 2019), pp. 239–244. ISSN: 0920-3206. DOI: 10.1007/s10557-019-06853-5. URL: http://link.springer.com/10.1007/s10557-019-06853-5.

[16] Patrizia Camelliti et al. "Adult human heart slices are a multicellular system suitable for electrophysiological and pharmacological studies". In: *Journal of Molecular and Cellular Cardiology* 51.3 (Sept. 2011), pp. 390–398. ISSN: 00222828. DOI: 10.1016/j.yjmcc.2011.06.018. URL: http://dx.doi.org/10.1016/j.yjmcc.2011.06.018%20https://linkinghub.elsevier.com/retrieve/pii/S0022282811002574.

[17] Samuel A. Watson et al. "Preparation of viable adult ventricular myocardial slices from large and small mammals". In: *Nature Protocols* 12.12 (2017), pp. 2623–2639. ISSN: 17502799. DOI: 10.1038/nprot.2017.139. URL: http://dx.doi.org/10.1038/nprot.2017.139.

[18] Carola Fischer et al. "Long-term functional and structural preservation of precision-cut human myocardium under continuous electromechanical stimulation in vitro". In: *Nature Communications* 10.1 (2019), pp. 1–12. ISSN: 20411723. DOI: 10.1038/s41467-018-08003-1. URL: http://dx.doi.org/10.1038/s41467-018-08003-1.

[19] Samuel A. Watson et al. "Biomimetic electromechanical stimulation to maintain adult myocardial slices in vitro". In: *Nature Communications* 10.1 (2019). ISSN: 20411723. DOI: 10.1038/s41467-019-10175-3.

[20] Jorik H Amesz et al. "Living myocardial slices: Advancing arrhythmia research". In: *Frontiers in Physiology* 14.January (Jan. 2023), pp. 1–9. ISSN:

1664-042X. DOI: 10.3389/fphys.2023.1076261. URL: https://www.frontiersin.org/articles/10.3389/fphys.2023.1076261/full.

[21] Alexandra Bussek et al. "Cardiac tissue slices with prolonged survival for in vitro drug safety screening". In: *Journal of Pharmacological and Toxicological Methods* 66.2 (Sept. 2012), pp. 145–151. ISSN: 10568719. DOI: 10.1016/j.vascn.2011.12.002. URL: http://dx.doi.org/10.1016/j.vascn.2011.12.002%20https://linkinghub.elsevier.com/retrieve/pii/S1056871911003236.

[22] Herbert M. Himmel et al. "Field and action potential recordings in heart slices: correlation with established in vitro and in vivo models". In: *British Journal of Pharmacology* 166.1 (May 2012), pp. 276–296. ISSN: 00071188. DOI: 10.1111/j.1476-5381.2011.01775.x. URL: https://onlinelibrary.wiley.com/doi/10.1111/j.1476-5381.2011.01775.x.

[23] Ken Wang et al. "Cardiac tissue slices: preparation, handling, and successful optical mapping". In: *American Journal of Physiology-Heart and Circulatory Physiology* 308.9 (May 2015), H1112–H1125. ISSN: 0363-6135. DOI: 10.1152/ajpheart.00556.2014. URL: https://www.physiology.org/doi/10.1152/ajpheart.00556.2014.

[24] Ramya Vijayakumar et al. "Methodology Considerations in Phase Mapping of Human Cardiac Arrhythmias". In: *Circulation: Arrhythmia and Electrophysiology* 9.11 (Nov. 2016), pp. 1–11. ISSN: 1941-3149. DOI: 10.1161/CIRCEP.116.004409. URL: https://www.ahajournals.org/doi/10.1161/CIRCEP.116.004409.

[25] Igor R. Efimov, Vladimir P. Nikolski, and Guy Salama. "Optical imaging of the heart". In: *Circulation Research* 95.1 (2004), pp. 21–33. ISSN: 00097330. DOI: 10.1161/01.RES.0000130529.18016.35.

[26] Vineesh Kappadan et al. "High-Resolution Optical Measurement of Cardiac Restitution, Contraction, and Fibrillation Dynamics in Beating vs. Blebbistatin-Uncoupled Isolated Rabbit Hearts". In: *Frontiers in Physiology* 11 (May 2020). ISSN: 1664-042X. DOI: 10.3389/fphys.2020.00464. URL: https://www.frontiersin.org/article/10.3389/fphys.2020.00464/full.

[27] Kieran E Brack et al. "The mechanical uncoupler blebbistatin is associated with significant electrophysiological effects in the isolated rabbit heart". In: 5 (2013), pp. 1009–1027. DOI: 10.1113/expphysiol.2012.069369.

[28] Andrew D. Bachtel et al. "A Novel Approach to Dual Excitation Ratiometric Optical Mapping of Cardiac Action Potentials With Di-4-ANEPPS Using Pulsed LED Excitation". In: *IEEE Transactions on Biomedical Engineering* 58.7 (July 2011), pp. 2120–2126. ISSN: 0018-9294. DOI: 10.1109/TBME.2011.2148719. URL: https://www.ncbi.nlm.nih.gov/pmc/articles/PMC3624763/pdf/nihms412728.pdf%0Afile:///C:/Users/ASUS/Desktop/Rujukan%20PhD/Dev%20of%20drug%20R%20cell%20line/nihms579608.pdf%20http://ieeexplore.ieee.org/document/5759733/.

[29] Gustavo K. Rohde, Benoit M. Dawant, and Shien Fong Lin. "Correction of motion artifact in cardiac optical mapping using image registration". In: *IEEE Transactions on Biomedical Engineering* 52.2 (2005), pp. 338–341. ISSN: 00189294. DOI: 10.1109/TBME.2004.840464.

[30] Hanyu Zhang et al. "Optical Mapping of Membrane Potential and Epicardial Deformation in Beating Hearts". In: *Biophysical Journal* 111.2 (2016), pp. 438–451. ISSN: 15420086. DOI: 10.1016/j.bpj.2016.03.043.

[31] E.L. Boulpaep. "Organization of the Cardiovascular System". In: *Medical Physiology*. Ed. by W.F. Boron and E.L. Boulpaep. 2nd ed. Elsevier Inc., 2012. Chap. 17, pp. 429–447.

[32] J.E. Hall. "Cardiac Muscle; The Heart as a Pump and Function of the Heart Valves". In: *Guyton and Hall Textbook of Medical Physiology*. 13th ed. saunders w.b., 2015. Chap. 9, pp. 109–122.

[33] E.L. Boulpaep. "The Heart as a Pump". In: *Medical Physiology*. Ed. by W.F. Boron and E.L. Boulpaep. 2nd ed. Elsevier Inc., 2012. Chap. 22, pp. 529–553.

[34] Richard N. Fogoros. "The Cardiac Electrical System". In: *Electrophysiologic testing*. 4th ed. Vol. 22. 1. Pittsburgh: Blackwell Publishing, 2006. Chap. 1, pp. 3–11. ISBN: 9781405104784. DOI: 10.1097/00003465-200301000-00003.

[35] W.J. Lederer. "Cardiac Electrophysiology and the Electrocardiogram". In: *Medical Physiology*. Ed. by W.F. Boron and E.L. Boulpaep. 2nd ed. Elsevier Inc., 2012. Chap. 21, pp. 504–528.

[36] Sergey F. Mironov, Frederick J. Vetter, and Arkady M. Pertsov. "Fluorescence imaging of cardiac propagation: spectral properties and filtering of optical action potentials". In: *American Journal of Physiology-Heart and Circulatory Physiology* 291.1 (July 2006), H327–H335. ISSN: 0363-6135. DOI: 10.1152/ajpheart.01003.2005. URL: https://www.physiology.org/doi/10.1152/ajpheart.01003.2005.

[37] E.D. Moczydlowski and M. Apkon. "Cellular Physiology of Skeletal, Cardiac, and Smooth Muscle". In: *Medical Physiology*. Ed. by W.F. Boron and E.L. Boulpaep. 2nd ed. Elsevier Inc., 2012. Chap. 9, pp. 237–266.

[38] David A. Eisner et al. "Calcium and Excitation-Contraction Coupling in the Heart". In: *Circulation Research* 121.2 (2017), pp. 181–195. ISSN: 15244571. DOI: 10.1161/CIRCRESAHA.117.310230.

[39] Donald M. Bers. "Cardiac excitation–contraction coupling". In: *Nature* 415.6868 (Jan. 2002), pp. 198–205. ISSN: 0028-0836. DOI: 10.1038/415198a. URL: http://www.nature.com/articles/415198a.

[40] Shaan Khurshid et al. "Frequency of Cardiac Rhythm Abnormalities in a Half Million Adults". In: *Circulation: Arrhythmia and Electrophysiology* 11.7 (2018), pp. 1–9. ISSN: 19413084. DOI: 10.1161/CIRCEP.118.006273.

[41] K et a. Lakshmi. "Epi of AF". In: *Neurologist* 14.3 (2008), pp. 143–150. DOI: 10.1097/NRL.0b013e31815cffae.Clinical.

[42] Emelia J. Benjamin et al. "Impact of Atrial Fibrillation on the Risk of Death". In: *Circulation* 98.10 (Sept. 1998), pp. 946–952. ISSN: 0009-7322. DOI: 10.1161/01.CIR.98.10.946. URL: https://www.ahajournals.org/doi/10.1161/01.CIR.98.10.946.

[43] Edit Tanai and Stefan Frantz. "Pathophysiology of Heart Failure". In: *Comprehensive Physiology*. Vol. 6. 1. Wiley, Dec. 2015, pp. 187–214. DOI: 10.1002/cphy.c140055. URL: https://onlinelibrary.wiley.com/doi/10.1002/cphy.c140055.

[44] Véronique L. Roger. "Epidemiology of Heart Failure". In: *Circulation Research* 113.6 (Aug. 2013), pp. 646–659. ISSN: 0009-7330. DOI: 10.1161/CIRCRESAHA.113.300268. URL: https://www.ahajournals.org/doi/10.1161/CIRCRESAHA.113.300268.

[45] J He. "Reduction in density of transverse tubules and L-type Ca2+ channels in canine tachycardia-induced heart failure". In: *Cardiovascular Research* 49.2 (Feb. 2001), pp. 298–307. ISSN: 00086363. DOI: 10.1016/S0008-6363(00)00256-X. URL: https://academic.oup.com/cardiovascres/article-lookup/doi/10.1016/S0008-6363(00)00256-X.

[46] Katharine M. Dibb et al. "Characterization of an Extensive Transverse Tubular Network in Sheep Atrial Myocytes and its Depletion in Heart Failure". In: *Circulation: Heart Failure* 2.5 (Sept. 2009), pp. 482–489. ISSN: 1941-3289. DOI: 10.1161/CIRCHEARTFAILURE.109.852228. URL: https://www.ahajournals.org/doi/10.1161/CIRCHEARTFAILURE.109.852228.

[47] A.M. Gómez et al. "Heart Failure After Myocardial Infarction". In: *Circulation* 104.6 (Aug. 2001), pp. 688–693. ISSN: 0009-7322. DOI: 10.1161/hc3201.092285. URL: https://www.ahajournals.org/doi/10.1161/hc3201.092285.

[48] Raimond L. Winslow et al. "Mechanisms of Altered Excitation-Contraction Coupling in Canine Tachycardia-Induced Heart Failure, II". In: *Circulation Research* 84.5 (Mar. 1999), pp. 571–586. ISSN: 0009-7330. DOI: 10.1161/01.RES.84.5.571. URL: https://www.ahajournals.org/doi/10.1161/01.RES.84.5.571.

[49] P. Camelliti, T Borg, and P Kohl. "Structural and functional characterisation of cardiac fibroblasts". In: *Cardiovascular Research* 65.1 (Jan. 2005), pp. 40–51. ISSN: 00086363. DOI: 10.1016/j.cardiores.2004.08.020. URL: https://academic.oup.com/cardiovascres/article-lookup/doi/10.1016/j.cardiores.2004.08.020.

[50] Peter Carmeliet and Rakesh K Jain. "Angiogenesis in cancer and other diseases". In: *Nature* 407.6801 (Sept. 2000), pp. 249–257. ISSN: 0028-0836. DOI: 10.1038/35025220. URL: www.nature.com%20http://www.nature.com/articles/35025220.

[51] M. H. Pincus. "Effect of Pitressin and Pitocin on Oxygen Consumption of Excised Tissue". In: *Experimental Biology and Medicine* 30.8 (May 1933), pp. 1171–1174. ISSN: 1535-3702. DOI: 10.3181/00379727-30-6843. URL: http://ebm.sagepub.com/lookup/doi/10.3181/00379727-30-6843.

[52] S. A. Watson et al. "A practical guide for investigating cardiac physiology using living myocardial slices". In: *Basic Research in Cardiology* 115.6 (Dec. 2020), p. 61. ISSN: 0300-8428. DOI: 10.1007/s00395-020-00822-y. URL: https://doi.org/10.1007/s00395-020-00822-y%20https://link.springer.com/10.1007/s00395-020-00822-y.

[53] Filippo Perbellini et al. "Investigation of cardiac fibroblasts using myocardial slices". In: *Cardiovascular Research* 114.1 (Jan. 2018), pp. 77–89. ISSN: 0008-6363. DOI: 10.1093/cvr/cvx152. URL: https://academic.oup.com/cardiovascres/article/114/1/77/4084720.

[54] Qinghui Ou et al. "Physiological Biomimetic Culture System for Pig and Human Heart Slices". In: *Circulation Research* (2020), pp. 628–642. ISSN: 15244571. DOI: 10.1161/CIRCRESAHA.119.314996.

[55] Yun Qiao et al. "Multiparametric slice culture platform for the investigation of human cardiac tissue physiology". In: *Progress in Biophysics and Molecular Biology* 144 (2019), pp. 139–150. ISSN: 00796107. DOI: 10.1016/j.pbiomolbio.2018.06.001.

[56] Omer Berenfeld and Igor Efimov. "Optical Mapping". In: *Cardiac Electrophysiology Clinics* 11.3 (2019), pp. 495–510. ISSN: 18779190. DOI: 10.1016/j.ccep.2019.04.004. URL: https://doi.org/10.1016/j.ccep.2019.04.004.

[57] Jacob I. Laughner et al. "Processing and analysis of cardiac optical mapping data obtained with potentiometric dyes". In: *American Journal of Physiology - Heart and Circulatory Physiology* 303.7 (2012). ISSN: 03636135. DOI: 10.1152/ajpheart.00404.2012.

[58] Kenneth R. Laurita et al. "Transmural Heterogeneity of Calcium Handling in Canine". In: *Circulation Research* 92.6 (Apr. 2003), pp. 668–675. ISSN: 0009-7330. DOI: 10.1161/01.RES.0000062468.25308.27. URL: https://www.ahajournals.org/doi/10.1161/01.RES.0000062468.25308.27.

[59] Pedro J. Del Nido et al. "Fluorescence measurement of calcium transients in perfused rabbit heart using rhod 2". In: *American Journal of Physiology-Heart and Circulatory Physiology* 274.2 (Feb. 1998), H728–H741. ISSN: 0363-6135. DOI: 10.1152/ajpheart.1998.274.2.H728. URL: https://www.physiology.org/doi/10.1152/ajpheart.1998.274.2.H728.

[60] Raghav Venkataraman et al. "Ratiometric imaging of calcium during ischemia-reperfusion injury in isolated mouse hearts using Fura-2". In: *BioMedical Engineering OnLine* 11.1 (Dec. 2012), p. 39. ISSN: 1475-925X. DOI: 10.1186/1475-925X-11-39. URL: https://biomedical-engineering-online.biomedcentral.com/articles/10.1186/1475-925X-11-39.

[61] Rafael Jaimes et al. "A technical review of optical mapping of intracellular calcium within myocardial tissue". In: *American Journal of Physiology - Heart and Circulatory Physiology* 310.11 (2016), H1388–H1401. ISSN: 15221539. DOI: 10.1152/ajpheart.00665.2015.

[62] Chikaya Omichi et al. "Intracellular Ca dynamics in ventricular fibrillation". In: *American Journal of Physiology-Heart and Circulatory Physiology* 286.5 (May 2004), H1836–H1844. ISSN: 0363-6135. DOI: 10.1152/ajpheart.00123.2003. URL: https://www.physiology.org/doi/10.1152/ajpheart.00123.2003.

[63] Jorge M. Davidenko et al. "Stationary and drifting spiral waves of excitation in isolated cardiac muscle". In: *Nature* 355.6358 (Jan. 1992), pp. 349–351. ISSN: 0028-0836. DOI: 10.1038/355349a0. URL: http://www.nature.com/articles/355349a0.

[64] Mark Warren et al. "Spatiotemporal Relationship Between Intracellular Ca 2+ Dynamics and Wave Fragmentation During Ventricular Fibrillation in Isolated Blood-Perfused Pig Hearts". In: *Circulation Research* 101.9 (Oct. 2007). ISSN: 0009-7330. DOI: 10.1161/CIRCRESAHA.107.162735. URL: https://www.ahajournals.org/doi/10.1161/CIRCRESAHA.107.162735.

[65] Di Lang et al. "Arrhythmogenic remodeling of β2 versus β1 adrenergic signaling in the human failing heart". In: *Circulation: Arrhythmia and Electrophysiology* 8.2 (2015), pp. 409–419. ISSN: 19413084. DOI: 10.1161/CIRCEP.114.002065.

[66] Stephen B. Knisley. "Transmembrane Voltage Changes During Unipolar Stimulation of Rabbit Ventricle". In: *Circulation Research* 77.6 (Dec. 1995), pp. 1229–1239. ISSN: 0009-7330. DOI: 10.1161/01.RES.77.6.1229. URL: https://www.ahajournals.org/doi/10.1161/01.RES.77.6.1229.

[67] Steven D. Girouard, Kenneth R. Laurita, and David S. Rosenbaum. "Unique properties of cardiac action potentials recorded with voltage- sensitive dyes". In: *Journal of Cardiovascular Electrophysiology* 7.11 (1996), pp. 1024–1038. ISSN: 10453873. DOI: 10.1111/j.1540-8167.1996.tb00478.x.

[68] William T. Baxter et al. "Visualizing Excitation Waves inside Cardiac Muscle Using Transillumination". In: *Biophysical Journal* 80.1 (Jan. 2001), pp. 516–530. ISSN: 00063495. DOI: 10.1016/S0006-3495(01)76034-1. URL: https://linkinghub.elsevier.com/retrieve/pii/S0006349501760341.

[69] David M. Jameson. "Absorption of Light". In: *Introduction to Fluorescence*. London: Taylor & Francis, 2014. Chap. 2, pp. 13–25.

[70] David M. Jameson. "Introduction". In: *Introduction to Fluorescence*. London: Taylor & Francis, 2014. Chap. 1, pp. 1–12.

[71] Joseph R Lakowicz. "Introduction to Fluorescence". In: *Principles of Fluorescence Spectroscopy*. 3rd ed. Baltimore: Springer, 2006. Chap. 1, pp. 1–25. ISBN: 0-387-31278-1.

[72] Jacobkhed. *Jablonski diagram of absorbance, non-radiative decay, and fluorescence*. 2002. URL: https://commons.wikimedia.org/wiki/File:Jablonski_Diagram_of_Fluorescence_Only.png.

[73] David M. Jameson. "Quantum Yields and Quencing". In: *Introduction to Fluorescence*. London: Taylor & Francis, 2014. Chap. 7, pp. 131–143.

[74] Joseph R. Lakowicz. "Fluorophores". In: *Principles of Fluorescence Spectroscopy*. 3rd ed. Baltimore: Springer, 2006. Chap. 3, pp. 63–94.

[75] Mina Attin and William T. Clusin. "Basic Concepts of Optical Mapping Techniques in Cardiac Electrophysiology". In: *Biological Research For Nursing* 11.2 (Oct. 2009), pp. 195–207. ISSN: 1099-8004. DOI: 10.1177/1099800409338516. URL: http://journals.sagepub.com/doi/10.1177/1099800409338516.

[76] Todd J. Herron, Peter Lee, and José Jalife. "Optical Imaging of Voltage and Calicum in Cardiac Cells & Tissues". In: *Circulation Research* 17.4 (2012), pp. 609–623. DOI: 10.1161/CIRCRESAHA.111.247494.Optical.

[77] Guy Salama and Seong-min Hwang. *Simultaneous Optical Mapping fo Intracellular Free Calcium and Action Potentials from Langendorff Perfused Hearts*. Vol. 176. 5. 2009, pp. 139–148. ISBN: 0000000000. DOI: 10.1002/0471142956.cy1217s49.Simultaneous.

[78] Christopher O'Shea et al. "High-Throughput Analysis of Optical Mapping Data Using ElectroMap". In: *Journal of Visualized Experiments* 2019.148 (June 2019), pp. 1–10. ISSN: 1940-087X. DOI: 10.3791/59663. URL: https://www.jove.com/t/59663/high-throughput-analysis-of-optical-mapping-data-using-electromap.

[79] Christopher O'Shea et al. "ElectroMap: High-throughput open-source software for analysis and mapping of cardiac electrophysiology". In: *Scientific Reports* 9.1 (Dec. 2019), p. 1389. ISSN: 2045-2322. DOI: 10.1038/s41598-018-38263-2. URL: http://www.nature.com/articles/s41598-018-38263-2.

[80] Jakub Tomek et al. "COSMAS: a lightweight toolbox for cardiac optical mapping analysis". In: *Scientific Reports* 11.1 (Dec. 2021), p. 9147. ISSN: 2045-2322. DOI: 10.1038/s41598-021-87402-9. URL: https://doi.org/10.1038/s41598-021-87402-9%20http://www.nature.com/articles/s41598-021-87402-9.

[81] Blake L. Cooper et al. "KairoSight: Open-Source Software for the Analysis of Cardiac Optical Data Collected From Multiple Species". In: *Frontiers in Physiology* 12.October (Oct. 2021), pp. 1–13. ISSN: 1664-042X. DOI: 10.3389/fphys.2021.752940. URL: https://www.frontiersin.org/articles/10.3389/fphys.2021.752940/full.

[82] Kandace Thomas et al. "Optical electrophysiology in the developing heart". In: *Journal of Cardiovascular Development and Disease* 5.2 (2018), pp. 1–19. ISSN: 23083425. DOI: 10.3390/jcdd5020028.

[83] Christopher O'Shea et al. "Cardiac Optogenetics and Optical Mapping – Overcoming Spectral Congestion in All-Optical Cardiac Electrophysiology". In: *Frontiers in Physiology* 10.MAR (Mar. 2019), pp. 1–14. ISSN: 1664-042X. DOI: 10.3389/fphys.2019.00182. URL: https://www.frontiersin.org/article/10.3389/fphys.2019.00182/full.

[84] Christine Grienberger and Arthur Konnerth. "Imaging Calcium in Neurons". In: *Neuron* 73.5 (2012), pp. 862–885. ISSN: 08966273. DOI: 10.1016/j.neuron.2012.02.011. URL: http://dx.doi.org/10.1016/j.neuron.2012.02.011.

[85] Mark Warren et al. "High-precision recording of the action potential in isolated cardiomyocytes using the near-infrared fluorescent dye di-4-ANBDQBS". In: *American Journal of Physiology - Heart and Circulatory Physiology* 299.4 (2010), pp. 1271–1281. ISSN: 03636135. DOI: 10.1152/ajpheart.00248.2010.

[86] P. Schaffer et al. "Di-4-ANEPPS causes photodynamic damage to isolated cardiomyocytes". In: *Pflügers Arch European Journal of Physiology* 426.6 (Apr. 1994), pp. 548–551. ISSN: 0031-6768. DOI: 10.1007/BF00378533. URL: http://link.springer.com/10.1007/BF00378533.

[87] Zhujiang Cao et al. "Registration of medical images using an interpolated closest point transform: method and validation". In: *Medical Image Analysis* 8.4 (Dec. 2004), pp. 421–427. ISSN: 13618415. DOI: 10.1016/j.media.2004.01.002. URL: https://linkinghub.elsevier.com/retrieve/pii/S1361841504000040.

[88] L.-Y Hsu and M.H Loew. "Fully automatic 3D feature-based registration of multi-modality medical images". In: *Image and Vision Computing* 19.1-2 (Jan. 2001), pp. 75–85. ISSN: 02628856. DOI: 10.1016/S0262-8856(00)00058-5. URL: https://linkinghub.elsevier.com/retrieve/pii/S0262885600000585.

[89] P.A. Van den Elsen et al. "Automatic registration of CT and MR brain images using correlation of geometrical features". In: *IEEE Transactions on Medical Imaging* 14.2 (June 1995), pp. 384–396. ISSN: 02780062. DOI: 10.1109/42.387719. URL: http://ieeexplore.ieee.org/document/387719/.

[90] P K Banerjee and A W Toga. "Image alignment by integrated rotational and translational transformation matrix". In: *Physics in Medicine and Biology* 39.11 (Nov. 1994), pp. 1969–1988. ISSN: 0031-9155. DOI: 10.1088/0031-9155/39/11/011. URL: https://iopscience.iop.org/article/10.1088/0031-9155/39/11/011.

[91] Lijun Ding et al. "Volumetric image registration by template matching". In: ed. by Kenneth M. Hanson. June 2000, pp. 1235–1246. DOI: 10.1117/12.387631. URL: http://proceedings.spiedigitallibrary.org/proceeding.aspx?articleid=923187.

[92] J.B.Antoine Maintz and Max A. Viergever. "A survey of medical image registration". In: *Medical Image Analysis* 2.1 (Mar. 1998), pp. 1–36. ISSN: 13618415. DOI: 10.1016/S1361-8415(01)80026-8. URL: https://linkinghub.elsevier.com/retrieve/pii/S1361841501800268.

[93] *Group 4: Image Fusion and Registration*. 2017. URL: https://wiki.tum.de/display/btt/Group+4%3A+Image+Fusion+and+Registration.

[94] Stephen B Knisley et al. "Ratiometry of transmembrane voltage-sensitive fluorescent dye emission in hearts". In: *American Journal of Physiology-Heart and Circulatory Physiology* 279.3 (Sept. 2000), H1421–H1433. ISSN: 0363-6135. DOI: 10.1152/ajpheart.2000.279.3.H1421. URL: https://www.physiology.org/doi/10.1152/ajpheart.2000.279.3.H1421.

[95] Elliot B. Bourgeois et al. "Simultaneous optical mapping of transmembrane potential and wall motion in isolated, perfused whole hearts". In: *Journal of Biomedical Optics* 16.09 (Sept. 2011), p. 1. ISSN: 1083-3668. DOI: 10.1117/1.3630115. URL: https://www.spiedigitallibrary.org/journals/journal-of-biomedical-optics/volume-16/issue-09/096020/Simultaneous-

optical-mapping-of-transmembrane-potential-and-wall-motion-in/10.1117/1.3630115.full.

[96] Arvydas Matiukas et al. "Near-infrared voltage-sensitive fluorescent dyes optimized for optical mapping in blood-perfused myocardium". In: *Heart Rhythm* 4.11 (Nov. 2007), pp. 1441–1451. ISSN: 15475271. DOI: 10.1016/j.hrthm.2007.07.012. URL: https://linkinghub.elsevier.com/retrieve/pii/S1547527107007163.

[97] Peter Lee et al. "In vivo ratiometric optical mapping enables high-resolution cardiac electrophysiology in pig models". In: *Cardiovascular Research* 115.11 (2019), pp. 1659–1671. ISSN: 17553245. DOI: 10.1093/cvr/cvz039.

[98] Peter Lee et al. "In Situ Optical Mapping of Voltage and Calcium in the Heart". In: *PLoS ONE* 7.8 (Aug. 2012). Ed. by Mathias Baumert, e42562. ISSN: 1932-6203. DOI: 10.1371/journal.pone.0042562. URL: https://dx.plos.org/10.1371/journal.pone.0042562.

[99] Arthur D Edelstein et al. "Advanced methods of microscope control using μManager software". In: *Journal of Biological Methods* 1.2 (Nov. 2014), e10. ISSN: 2326-9901. DOI: 10.14440/jbm.2014.36. URL: https://jbmethods.org/jbm/article/view/36.

[100] Jorik Amesz and Yannick Taverne. "Working Protocol Myocardial Slices for Biomimetic System Culture". In: (2022), pp. 1–16.

[101] S. Klein et al. "elastix: A Toolbox for Intensity-Based Medical Image Registration". In: *IEEE Transactions on Medical Imaging* 29.1 (Jan. 2010), pp. 196–205. ISSN: 0278-0062. DOI: 10.1109/TMI.2009.2035616. URL: http://ieeexplore.ieee.org/document/5338015/.

[102] Denis Shamonin. "Fast parallel image registration on CPU and GPU for diagnostic classification of Alzheimer's disease". In: *Frontiers in Neuroinformatics* 7 (2013). ISSN: 16625196. DOI: 10.3389/fninf.2013.00050. URL: http://journal.frontiersin.org/article/10.3389/fninf.2013.00050/abstract.

[103] *pE-300ultra*. URL: https://www.coolled.com/products/pe-300ultra/.

[104] Kara Garrott et al. "K ATP channel inhibition blunts electromechanical decline during hypoxia in left ventricular working rabbit hearts". In: *The Journal of Physiology* 595.12 (June 2017), pp. 3799–3813. ISSN: 00223751. DOI: 10.1113/JP273873. URL: https://onlinelibrary.wiley.com/doi/10.1113/JP273873.

[105] Christopher J. Hyatt et al. "Optical Action Potential Upstroke Morphology Reveals Near-Surface Transmural Propagation Direction". In: *Circulation Research* 97.3 (Aug. 2005), pp. 277–284. ISSN: 0009-7330. DOI: 10.1161/01.RES.0000176022.74579.47. URL: https://www.ahajournals.org/doi/10.1161/01.RES.0000176022.74579.47.

[106] Iain Sim et al. "Left atrial voltage mapping: defining and targeting the atrial fibrillation substrate". In: *Journal of Interventional Cardiac Electrophysiology* 56.3 (Dec. 2019), pp. 213–227. ISSN: 1383-875X. DOI: 10.1007/s10840-019-00537-8. URL: http://link.springer.com/10.1007/s10840-019-00537-8.

[107] Peter Lee et al. "Low-Cost Optical Mapping Systems for Panoramic Imaging of Complex Arrhythmias and Drug-Action in Translational Heart Models". In: *Scientific Reports* 7.February (2017), pp. 1–14. ISSN: 20452322. DOI: 10.1038/srep43217.

[108] Jan Christoph and Stefan Luther. "Marker-Free Tracking for Motion Artifact Compensation and Deformation Measurements in Optical Mapping Videos of Contracting Hearts". In: *Frontiers in Physiology* 9.NOV (Nov. 2018). ISSN:

1664-042X. DOI: 10.3389/fphys.2018.01483. URL: https://www.frontiersin.org/article/10.3389/fphys.2018.01483/full.

[109] CoolLED. *Measuring illumination intensity with accuracy and precision*. Tech. rep. URL: https://www.coolled.com/whitepapers/measuring-illumination-intensity-with-accuracy-and-precision/.

[110] Ruirui Dong et al. "A protocol for dual calcium-voltage optical mapping in murine sinoatrial preparation with optogenetic pacing". In: *Frontiers in Physiology* 10.JUL (2019). ISSN: 1664042X. DOI: 10.3389/fphys.2019.00954.

[111] Sharon A. George, Jaclyn A. Brennan, and Igor R. Efimov. "Preclinical cardiac electrophysiology assessment by dual voltage and calcium optical mapping of human organotypic cardiac slices". In: *Journal of Visualized Experiments* 2020.160 (2020), pp. 1–17. ISSN: 1940087X. DOI: 10.3791/60781.

[112] di Lang et al. "Optical mapping of action potentials and calcium transients in the mouse heart". In: *Journal of Visualized Experiments* 2.55 (2011), pp. 1–6. ISSN: 1940087X. DOI: 10.3791/3275.

[113] Christopher O'Shea et al. "High resolution optical mapping of cardiac electrophysiology in pre-clinical models". In: *Scientific Data* 9.1 (Dec. 2022), p. 135. ISSN: 2052-4463. DOI: 10.1038/s41597-022-01253-1. URL: https://www.nature.com/articles/s41597-022-01253-1.

MATLAB code

A

This appendix contains a step-by-step description of the MATLAB code used throughout the thesis.

A.1 Ratiometric Imaging Control

To achieve ratiometric imaging, a voltage output module is used to send TTL pulses to the camera and LED system. The voltage output module has to be detected by MATLAB, after which it is possible to use the module to send a pulse train to the LED system and camera. The *LED_CAM_control.m* script is used.

A.1.1 Finding the Voltage Output Module

First, the voltage output module needs to be detected using `daqlist`. Next, the `daq` command creates a `DataAcquisition` object containing information that describes the hardware.

```
%% Finding Voltage Output Module
dl = daqlist('ni')
dq = daq('ni')
```

The NI-9263 voltage output module has four output channels, three of which are used for ratiometry. These channels can be added with the command `addinput`.

```
addoutput(dq,'cDAQ1Mod1', 'ao0', 'Voltage');
addoutput(dq,'cDAQ1Mod1', 'ao1', 'Voltage');
addoutput(dq,'cDAQ1Mod1', 'ao2', 'Voltage');
```

Now, output channels AO0, AO1, and AO2 from the NI-9263 voltage output module are ready to use.

A.1.2 Pulse Train

When the NI-9263 voltage output module is recognized and the output channels are added, a pulse train can be sent. The camera needs to reach a steady state of 2000 fps. It can take up to 40 s to reach this steady state. Therefore, `n_pulse` is set to 100000 (50 s).

The recording duration depends on the pacing frequency of the LMS. To ensure that a whole AP is recorded, the recording duration should be at least twice as long as the interval between two pacing stimuli. At a pacing frequency of 1 Hz, this translates to a recording of at least 2 seconds. To reach a frame rate of 2000 fps, the voltage output rate (`dq.Rate`) is set to 2000, multiplied by the sampling rate (`sampling`).

```
%% Pulse train
% for pacing freq. of 1Hz (60 bpm):
% recording duration is 2 seconds to ensure the
% recording of at least one whole contraction.
% At 2000 fps, this results in 4000 frames.

n_pulse = 100000;                   % number of pulses to send
sampling = 10;
t = 0:1/sampling:n_pulse;           % steps at which the function
                                    % is evaluated
dq.Rate = 2000*sampling;            % output rate of NI-9263
```

The pulse trains for the LEDs and the camera are generated with the function `plustran`. With `@rectpuls`, a rectangular pulse is generated. Two pulse trains are generated to control the LEDs. These pulse trains run out of phase, with a step size of 2 (`d` and `d2`). To ensure that the slice is not illuminated longer than necessary, `d` starts at `n_pulse = 60000.5`, and `d2` starts at `n_pulse = 59999.5`. Thus, illumination begins approximately 30 *s* after the camera is started. A third pulse train controls the camera frame rate. This pulse train has a step size of 1 (`d3`) and is in phase with both of the LED pulse trains.

```
x = @rectpuls;                      % block pulse

% pulse train steps
d = [60000.5:2:n_pulse];
d2 = [59999.5:2:n_pulse];
d3 = [0:1:n_pulse];
```

A sampling frequency is set for each pulse train. For the LEDs, this is 0.9 (`fs` and `fs2`), ensuring that the two LEDs are not turned on at the same time. The sampling rate of the camera is set to 0.25 (`fs3`) to ensure that the camera is solely turned on during LED illumination. `y`, `y2`, and `y3` are the pulse trains for the red LED, blue LED, and camera, respectively.

```
% sampling frequency
fs = 0.9;
fs2 = 0.9;
fs3 = 0.25;

% pulse train generation
y = pulstran(t,d,x,fs);             % output channel 1(AO1): red LED
y2 = pulstran(t,d2,x,fs2);          % output channel 2(AO2): blue LED
y3 = 1-pulstran(t,d3,x,fs3);        % output channel 3(AO3): camera
```

An output signal (`outputSignal`) of 5 *V* is generated and sent to the corresponding voltage output channel.

```
%% Voltage Output
outputSignal = [5*y; 5*y2; 5*y3]';
write(dq, outputSignal)
```

A.2 Filtering

Preprocessing and marker segmentation are performed with the matlab script *preprocessing_LMS.m*. Filtering consists of loading the desired *.tiff* file into MATLAB as a 3D array (`img`). The frames are scaled with `rescale` to increase the overall intensity, resulting in another 3D array: `scale_img`.

```
%% Load recording, adjust intensity
img = tiffreadVolume("test_run1_8_MMStack_Default.ome.tif");
scale_img = rescale(double(img));
```

The function `fspecial` is used to create a 2D filter to smooth the images. A disk-shaped filter with a radius of $r = 3$ is used.

```
disk = fspecial('disk',3);
img_filt = imfilter(scale_img, disk, 'replicate');
```

A sliceviewer pops up to show the resulting filtered images, along with the question of whether the first frame is bright [B] (blue illuminated) or dark [D] (red illuminated). Depending on the answer to the question, the first frame is removed so that the first frame is always a 480 *nm* illuminated frame.

```
figure,
S = sliceViewer(img_filt)

pause

prompt_slice = ['Is the first frame bright [B] or dark [D]? '];
prompt_slice_ans = input(prompt_slice,'s');
if prompt_slice_ans=='b' || prompt_slice_ans=='B'
    prompt_slice_ans='B'
elseif prompt_slice_ans=='d' || prompt_slice_ans=='D'
    prompt_slice_ans='D'
    img(:,:,1) = [];
    scale_img(:,:,1) = [];
    img_filt(:,:,1) = [];
    fprintf('Removing first frame.')
else
    fprintf('Invalid input on question!')
end
```

A.3 Motion Correction

Robust, affine motion correction is performed. This is followed by ratiometric artefact reduction.

A.3.1 Marker Segmentation

Preprocessing and marker segmentation are performed with the matlab script *preprocessing_LMS.m* as well. Before motion correction is performed, the data is separated into two image arrays: blue-illuminated frames, and red-illuminated frames.

```
%% Isolating blue and red illuminated frames
for i = 1:size(img,3)
    if mod(i,2) ==0;                % even slices, red
        img_even (:,:,i/2) = img_filt(:,:,i);
    else mod(i ,2) ≠0;              % odd slices, blue
        img_odd (: ,: ,(i+1)/2) = img_filt(:,:,i);
    end
end
```

To segment the markers, a threshold is manually chosen, based on the pixel intensity of the markers in `img_filt`. The first frame if `img_filt` is shown. The *Data Tip* should be used to determine the threshold.

```
%% Marker segmentation
figure, imshow(img_filt(:,:,1))
title 'Use the Data Tip to find a proper threshold'
pause
```

Once the threshold is found, a prompt asks to enter the value of the threshold. The threshold is used to create a binary image in which the pixels with a value lower than the threshold remain in the array `thres`. Objects touching the edges of the frame are removed with `imclearborder`.

```
for i = 1:size(img_odd,3)
    thres(:,:,i) = img_odd(:,:,i)<threshold;
    clear_border(:,:,i) = imclearborder(thres(:,:,i));
end
```

An overlay of the first frame and a robust marker segmentation is shown. The cursor is used to select the four objects that represent the markers.

```
figure, imshow(labeloverlay(img_filt(:,:,1),clear_border(:,:,1)))
title 'Get coordinates for center of each marker'
[x,y] = getpts;
```

The function `bwselect` is used to select the four objects (`BW1`, `BW2`, `BW3`, and `BW4`) per frame that represent the markers. `bwselect` does this, based on coordinates that are manually entered after examining several frames from `thres`. A mask with the markers is created by combining `BW1`, `BW2`, `BW3`, and `BW4` into `mask`.

```
for i = 1:size(img_odd,3)
    BW1(:,:,i) = bwselect(clear_border(:,:,i),x(1),y(1));
    BW2(:,:,i) = bwselect(clear_border(:,:,i),x(2),y(2));
    BW3(:,:,i) = bwselect(clear_border(:,:,i),x(3),y(3));
    BW4(:,:,i) = bwselect(clear_border(:,:,i),x(4),y(4));
    mask(:,:,i) = BW1(:,:,i)+BW2(:,:,i)+BW3(:,:,i)+BW4(:,:,i);
end
```

The success of the marker segmentation is determined by finding the number of objects in each layer of array `mask`. If the number of objects is lower than four, the segmentation for this frame has failed. The positions of the failed masks are saved in `failed_mask`.

```
%% Replacing outliers
for i = 1:size(img_odd,3)
    cc(i) = bwconncomp(mask(:,:,i),4);
    no_markers(i) = cc(1,i).NumObjects;
end

failed_mask = find(no_markers<4)
```

The failed masks are replaced by their preceding mask in `mask`. It is checked whether the number of failed masks is zero after this operation by checking whether `failed_mask_rep` is an empty array.

```
 for i = 1:length(failed_mask);
    for k = failed_mask(i)
        mask(:,:,k) = mask(:,:,k-1);
    end
end

for i = 1:size(img_even,3)
    cc_mask(i) = bwconncomp(mask(:,:,i),4);
    no_markers_mask(i) = cc_mask(1,i).NumObjects;
end

failed_mask_rep = find(no_markers_mask<4)
```

The output is saved as a .mat-file.

```
    save('marker_seg.mat', 'img', 'scale_img', 'img_filt', 'mask',
    'img_even', 'img_odd')
```

A.3.2 Image Registration

The script *registration_markers.m* is used in this section. The data, saved in the previous section is loaded into MATLAB again.

```
%% Marker registration
load('marker_seg.mat')
```

The marker segmentations (`mask`) are assigned `fixed` and `moving`. `fixed` consists of the first frame of `mask`, `moving` consists of the remaining layers of `mask`.

```
fixed = imcomplement(double(mask(:,:,1)));
for i = 2:size(mask,3)
        moving(:,:,i-1) = imcomplement(double(mask(:,:,i-1)));
end
```

A temporary directory is created for the registration data, in order to extract the transformation matrix. The transformation matrix will be used to perform image registration of the frames.

```
for i = 2:size(moving,3)
    tmpDir{i} = fullfile(tempdir,'registrations');
end
```

Elastix is used to perform image registration. Since the markers are very small, the number of spatial samples is set to the size of the `fixed` array. The registered frames (`regim`), registration parameters (`regparm`), and transformation matrix (`invert_t`) are extracted.

```
for i = 2:size(moving,3)
    modifierStruct.Interpolator='NearestNeighborInterpolator';
    modifierStruct.FixedImageDimension=2;
    modifierStruct.MovingImageDimension=2;
    modifierStruct.NumberOfSpatialSamples = 3000;
    modifierStruct.MaximumNumberOfIterations = 500;
    modifierStruct.Optimizer = 'AdaptiveStochasticGradientDescent';
    [regim{i},regparm{i}] = elastix(moving(:,:,i),fixed,tmpDir{i},...
    'elastix_default.yml','paramstruct', modifierStruct);
    invert_t{i} = invertElastixTransform(regparm{i}.outputDir);
end
```

Once the registration is performed, based on the markers. The transformation matrix, saved in `invert_t`, is used to register the full frames. The transformation of the blue illuminated frames is duplicated to also serve as the transformation of the preceding red illuminated frames.

```
for i = 1:2*length(invert_t)
    if mod(i,2)==0;
        trans_matrix{i} = invert_t{i/2};
    else mod(i,2)≠0;
        trans_matrix{i} = invert_t{(i+1)/2};
    end
end
```

Now, the transformation can be applied to the original data

```
reg_slice(:,:,1) = img(:,:,1);
for i = 2:3999
    reg_slice(:,:,i) = transformix(img(:,:,i), trans_matrix{i-1});
end
```

This results in the array `reg_slice` with the first frame being the fixed image. All the other images are transformed to this image with a transformation matrix, based

on the previously acquired marker segmentations. These parameters are saved as well.

```
save('final_reg.mat', 'regim', 'regparm', 'modifierStruct',
'invert_t', 'moving', 'fixed', 'reg_slice', 'trans_matrix')
```

A.3.3 Ratiometry

For this section, *ratiometry.m* is used. A ROI is cropped from the LMS after image registration to ensure that the same area is used for ratiometric correction. An area is cropped from the first blue-illuminated frame.

```
[x, rect] = imcrop(reg_slice(:,:,2))
```

The same area is also cropped from every other frame. The cropped frames are also rescaled and filtered.

```
for i = 2:size(img_filt,3);
    crop(:,:,1) = x;
    crop(:,:,i) = imcrop(reg_slice(:,:,i),rect);
end

scale_crop = rescale(crop);
disk = fspecial('disk', 2);
crop_filt = imfilter(scale_crop, disk, 'replicate');
```

To perform ratiometric correction, the average of two subsequent red-illuminated images (`av_r`) was taken, and this was divided by its intermediate blue-illuminated image.

```
for i = 3:2:size(crop_filt,3)
    for j = i/2 -0.5
        av_r(:,:,j) = (crop_filt(:,:,i-1)+crop_filt(:,:,i+1))./2;
        ratio_b(:,:,j) = av_r(:,:,j)./crop_filt(:,:,i);
    end
end
```

The output after ratiometric correction (`ratio_b`) was saved ar a *.tiff* file with the following code:

```
imwrite(ratio_b(:,:,1), 'ratio.tif');
for i = 2:size(ratio_b,3)
    imwrite(ratio_b(:,:,i), 'ratio.tif', 'WriteMode', 'append');
end
```

Workprotocol Optical Mapping

B

B.1 Preparation

Preparation of optical mapping experiments consists of several steps. For the preparation of LMS and *culture medium*, consult *Working Protocol Myocardial Slices for Biomimetic System Culture* [100].

B.1.1 Preparation of Solutions

1. Prepare *dye stock* by dissolving di-4-ANBDQBS in 100% ethanol to obtain 10 mM stock solution
    a. Dissolve 100 nmol (1 tube) of di-4-ANBDQBS by adding 0.01 ml ethanol, using a micropipette
    Resulting in 0.01 ml 10 of mM *dye stock*
    b. Vortex and spin the contents of the tube
    Dye stock can be stored at $-20°C$

B.1.2 Dye Loading

1. Dilute *dye stock* to 42 µM in *culture medium* (*dye solution*)
    a. Dilute the 0.01 ml *dye stock* to a 2.4 ml *dye solution* by adding 2.39 ml culture medium, using a micropipette
    b. Mix *dye solution* by suctioning and pipetting 0.8 ml *dye solution* multiple times
2. Heat the *dye solution* to $37°C$ in a water bath
3. Take a culture dish out of the incubator
4. Remove *culture medium* from the culture dish
5. Replace the medium in the culture dish with the 2.4 ml of *dye solution* and stain the cells for 30 min at $37°C$ in the incubator
6. Wash out the *dye solution*
    a. Using a pipette, remove the *dye solution* from the culture dish

b. Add 0.8 ml of *culture medium* to the culture dish, and remove this again, repeat 3-5 times to wash out any excess *dye solution*

7. Add 2.4 ml *culture medium* to the culture dish
8. Rub the lid of the culture dish with Ultrastop to prevent condensation on the lid
9. Place the culture dish in the incubator to reheat to 37°C

B.2 Optical Mapping

1. Heat optical mapping system to 37°C by turning on the WarmAir Hyperthermia System (system on the floor, see *Figure* B.1). Temperature can be checked with the thermocouple on top of the optical mapping system (*can take up to 30 min!*)

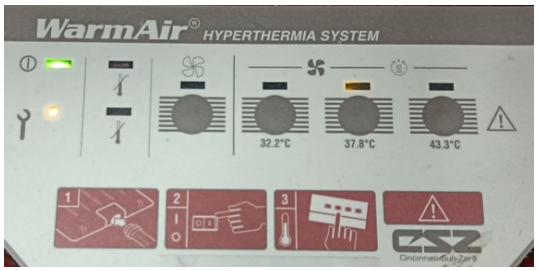

FIGURE B.1: Control panel of WarmAir Hyperthermia System

2. Start the computer
3. Open MATLAB and run Section 1 and Section 2 from *LED_CAM_control.m* (*this takes a while!*)
4. Place a pacing plate in the optical mapping system and attach the power supply and USB cable
5. Open MyoDish software
6. Reposition the LED collimator so that it is as close to the camera lens as possible to illuminate the desired culture dish position (A, B, C, or D) directly underneath the camera lens (see *Figure* B.2).

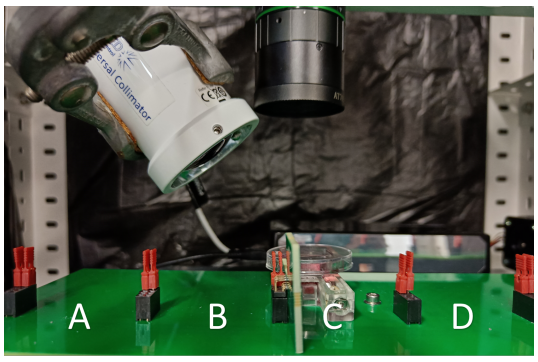

FIGURE B.2: Example of collimator placement to illuminate culture dish position C

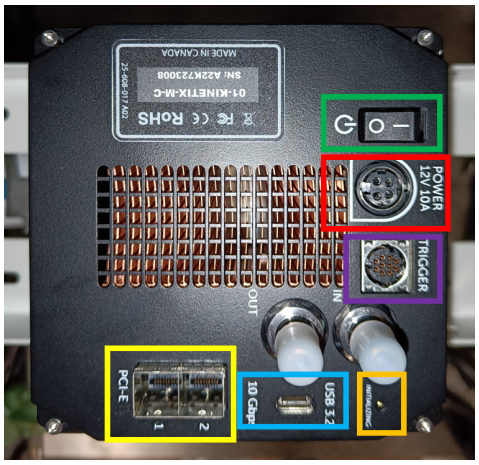

(A) Top side of the camera. Green box: on/off button, red box: power supply, purple box: trigger, yellow box: PCIe data ports, blue: USB3.2, orange box: initialization LED

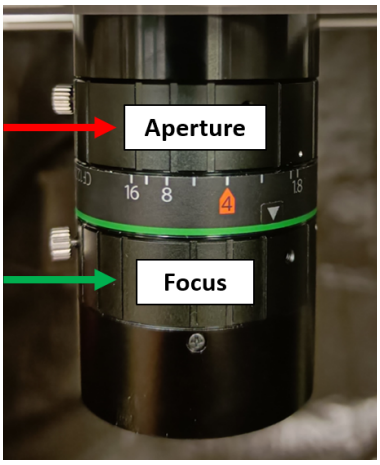

(B) Lens with the red arrow showing the top wheel: aperture adjustment, and the green arrow pointing to the bottom wheel: lens focus adjustment

FIGURE B.3: Top view of the camera and side view of the camera lens

7. Check whether all the cables are connected to the camera and turn on camera, see *Figure* B.3a
8. Wait for the orange initialization LED to stop blinking before proceeding
9. Open the *Micro-Manager 2.0* app on Desktop, see *Figure* B.4
   a. Select *Default User* as user
   b. Chose *KINETIX&pE-300ultra.cfg* as Hardware Configuration File

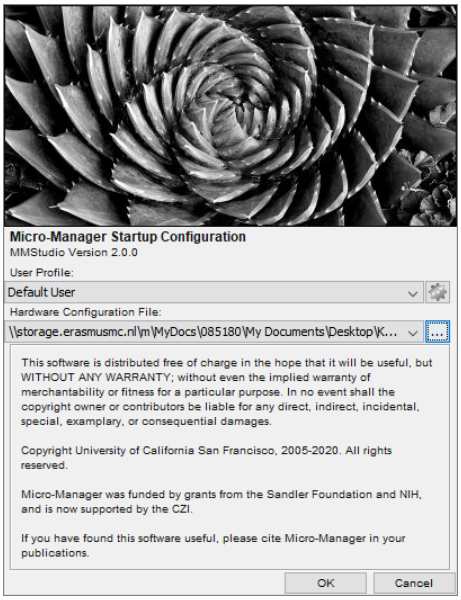

FIGURE B.4: Micro-Manager 2.0 Home Screen

10. Position the LMS (in a culture dish, on a biomimetic pacing plate) directly underneath the camera lens and continue rocking and pacing at 1 *Hz*, 50 *mA*
11. Adjust camera settings, see *Figure* B.5

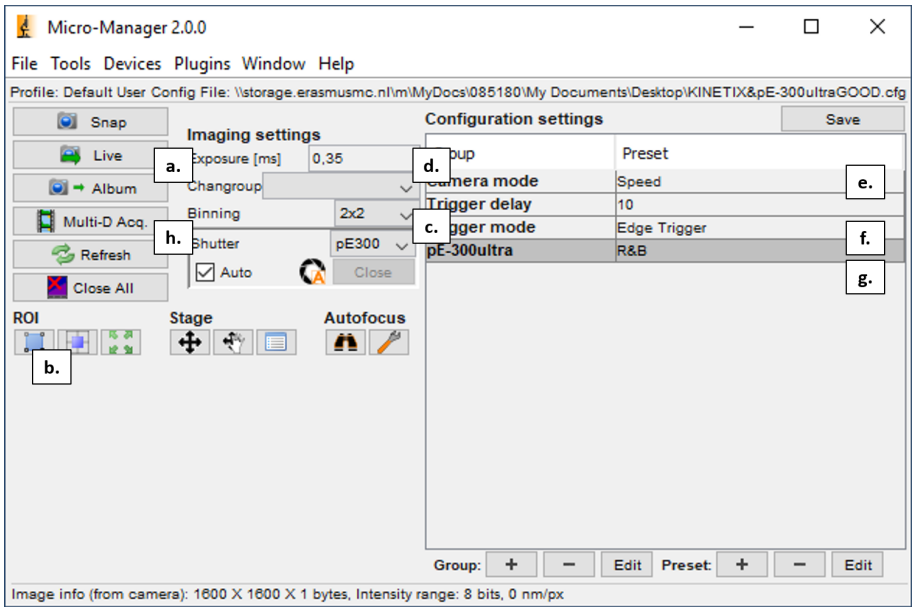

FIGURE B.5: Micro-Manager 2.0 Main Window

a. Press Live. A live feed of the camera will appear in black-and-white
If you see a completely black screen, rotate the top wheel of the lens counterclockwise to increase the lens aperture, see *Figure* B.3b

b. Zoom out on the live feed. Select a region of interest (ROI) with the cursor. Ensure that the LMS and its plastic triangles are fully in the ROI. Press the button at b. to confirm your ROI
Check that the ROI is not bigger than 260x260px (the right top corner of the live feed)

c. Using the drop-down menu at c., set *Binning* to 2x2

d. Set *Exposure time [ms]* to 0,35 at d.

e. Check whether *Camera mode* is set to *Speed* at e.. Check the camera frame rate at the right bottom of the live feed. This should be > 2000 fps

f. At f., set *Trigger mode* to *Edge Trigger*

12. Pause rocking temporarily to adjust the zoom and aperture of the lens (for this, you need *Trigger mode* in the setting *Internal Trigger*)

13. Adjust the focus by rotating the bottom wheel of the lens
Use the top wheel (aperture) of the lens to adjust the amount of light coming in, see *Figure* B.3b

14. Screw the emission filter on the lens

15. Adjust the lens aperture for optical mapping, see *Figure* B.3b:

- Turn on blue led by selecting *480nm* in the drop-down menu at g.
- Rotate the top wheel of the lens until the LMS is visible
- Switch to red light by selecting *640nm* in the drop-down menu at g. and control whether the LMS is still visible

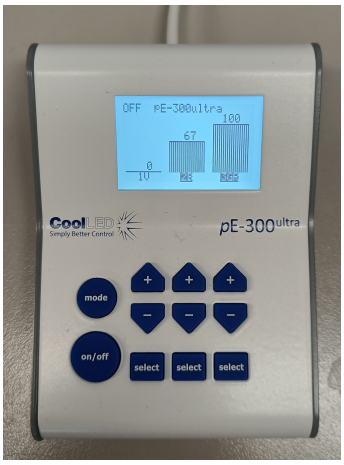

FIGURE B.6: Caption

If not, slightly adjust the top wheel of the lens
Repeat steps until the LMS is visible when the blue light is turned on, and when the red light is turned on

16. Once the camera settings are finalized, turn off the light at g., close the door of the optical mapping system and continue rocking
17. At h., press Multi-D Acq.
18. Set a save-directory
19. Go back to MATLAB and run Section 3 of *CAM_LED_control.m* in MATLAB
20. Directly press Live on the live feed, the number in the right bottom corner should slowly decrease to 2000 fps
21. Turn off the illumination by pressing the round button that says *on/off* (see *Figure* B.6). Illumination will automatically turn on again after 30 *s* through TTL-pulses
22. Stop rocking
23. Once the frame rate has reached 2000 fps, press **Acquire!** in the Multi-Dimensional Acquisition window
24. After recording, continue rocking
25. Close the recording and rename it to include the variables: *#frames_pixel binning_frame rate_type of illumination_additional information*